이학박사 학위논문

Molecular Dynamics Simulation Study of Room-Temperature Ionic Liquids:
Dynamic Heterogeneity and Solvation Dynamics
이온성 액체에 대한 분자 동력학 전산모사 연구: 동력학적 불균일성과 용매화 과정

2016년 8월

서울대학교 대학원
화학부 물리화학 전공
김 대 건

Molecular Dynamics Simulation Study of Room-Temperature Ionic Liquids:
Dynamic Heterogeneity and Solvation Dynamics

지도교수 정 연 준

이 논문을 이학박사 학위논문으로 제출함
2016년 7월
서울대학교 대학원
화학부 물리화학 전공
김 대 건

김대건의 이학박사 학위논문을 인준함
2016년 6월

위 원 장	석 차 옥	(인)
부위원장	정 연 준	(인)
위 원	이 상 엽	(인)
위 원	성 봉 준	(인)
위 원	심 영 선	(인)

Abstract

In this thesis, we study dynamics of room-temperature ionic liquids using computational method. At first, we investigate the dynamic propensity in a coarse-grained model of a room-temperature ionic liquid. Dynamic propensity is defined as the average of squared displacements for each ion during a given time interval over the isoconfigurational ensemble. As the temperature is lowered, distributions of the dynamic propensity develop fat tails at high values, indicating the presence of dynamic heterogeneity in the system. The increase in the heterogeneity for the cation is more evident than that for the anion, and a high propensity exhibits a large variance in the isoconfigurational ensemble, implying that dynamic propensity is related to ions' motions at a large length scale, rather than a direct measure of the individual ion dynamics. In addition, large non-Gaussian parameters observed for small dynamic propensities reveal intermittent dynamical behaviors of ions. In order to reveal the origin of the dynamic heterogeneity in a room-temperature ionic liquid, a possible correlation between the mobility and dynamic propensity is further probed. It is observed that spatial distributions of the dynamic propensity coincide with those of the mobility. The results suggest a possible connection between the structure and

heterogeneous dynamics on large length scales.

In the second part of this thesis, we study how the excitation energy affects the dynamic properties and the emission spectrum of solvation in 1-ethyl-3-methylimidazolium hexafluorophosphate ($EMI^+PF_6^-$) by performing the molecular dynamics simulations on its coarse-grained model. We use very narrowly distributed excitation energies unlike former studies where excitation energy was expressed in an averaged way from a distribution. The isoconfigurational ensemble method enables this sampling with a reliable statistics. Using that, we calculate the Stokes shift function, $S(t)$, to show that its relaxation becomes slower with the lower excitation energy, converging to the equilibrium correlation function, $C(t)$, of the solvation energy fluctuation, implying that the red-shifted system approaches the linear response regime. We also analyze variances of solvation energy between nonequilibrium trajectories to verify that the effect of initial configuration is profound at short time, $\sim$1 ps, and diminishes with time passing by whereas that of velocity dominates at long time. We also calculate the emission spectrum showing the red-edge effect, consistently with previous studies.

Keywords: room-temperature ionic liquid, dynamic heterogeneity, isoconfigurational ensemble, coarse-grained model, dynamic propensity, solvation dynamics, Stokes-shift function, red-edge effect, molecular dynamics simulation

Student Number: 2007-20295

Contents

List of Figures

List of Tables

Chapter 1

Overview

1.1 Room-temperature ionic liquid and dynamic heterogeneity

In recent years, room-temperature ionic liquids (RTILs) have attracted considerable interest due to their unique properties. Their negligible vapor pressure and renewable nature makes them an environmentally greener reaction media as opposed to other toxic organic solvents.[1] Moreover, due to their wide range of solubility, miscibility with a polar and a non-polar solvent, high ionic conductivity and thermal stability, RTILs have attracted much attention as a novel class of solvent for various chemical reactions and applications.[2] RTILs are commonly composed of bulky and asymmetric cations, such as *N*,*N*'-dialkylimidazolium and *N*-alkylphiridinium, and small anions, such as hexafluorophosphate (PF_6^-), tetrafluoroborate (BF_4^-), nitrate (NO_3^-), triflate (TfO^-), and halide. RTILs are organic salts which exist a liquid state at an ambient temperature due to the size difference between a cation and an anion. This size difference also induces

another important property of RTILs, so called dynamic heterogeneity.

Dynamic heterogeneity which is originally introduced in supercooled liquid system refers to the occurrence of temporal and spatial fluctuation in the local dynamics as the temperature decreases. Dynamic heterogeneity, which is usually observed in most disordered system with glassy dynamics, is characterized by various unique properties, such as subdiffusive behavior at the intermediate time scale, non-exponential decay of structural relaxation, the violation of Stokes-Einstein relation, and decoupling of exchange times and persistence times. [3–9] One of the model systems which describes well these interesting features is kinetically constrained model (KCM) based on the dynamic constraint. Binary Lennard-Jones (LJ) mixture and Weeks-Chandler-Anderson mixture can also reproduce many dynamic properties of supercooled liquid systems. Meanwhile, similar behaviors with those of supercooled liquid systems are also observed in RTILs, although they have quite different properties from the LJ mixture, such as complex molecular structure and Coulomb interaction between ions. [10] With this respect, we study dynamic heterogeneity of RTIL system applying one of a methodology, isoconfigurational ensemble, already used in supercooled liquid system in order to explore the possible correlation between dynamic heterogeneity and the structure.

1.2 Outline of the thesis

In this thesis, dynamic heterogeneity and solvation dynamics of RTILs are studied *via* molecular dynamics simulation method. The key concepts of this thesis, isoconfigurational ensemble and coarse-grained model, are introduced in Section 1.3 and Section 1.4, respectively. In Section 1.5, we briefly introduce solvation dynamics. In Chapter 2, dynamic propensity will be introduced to quantify the dynamic heterogeneity of RTILs. We will demonstrate how the initial structure influences the subsequent dynamics through statistically quantitative analysis of dynamic propensity. Another dynamical study of RTILs, that is, study of solvation dynamics will be discussed in Chapter 3. In this chapter, we will show the excitation-energy dependence of nonequilubrium relaxation and steady-state emission spectrum of solvation dynamics.

1.3 Isoconfigurational ensemble method

Isoconfigurational ensemble method is proposed by Harrowell and coworkers[11–13] in order to find a structure-dynamics correlation, especially the effects of initial configuration on the subsequent dynamics, in a supercooled liquid system. If there is no correlation at all between an initial configuration and the following dynamics of the system, an averaged particle's quantity over many trajectories with the same initial configuration would be the same as that of every other particles regardless of the position of particle in the system. Unexpected variation of different initial velocity distributions among the trajectories vanishes by averaging over the large number of trajectories. On the contrary, if the averaged quantity shows a clear distinction between different particles, it is a significant evidence which demonstrates the influence of initial configuration on later dynamics. In this regard, isoconfigurational ensemble consist of trajectories which have same initial configuration, while the initial velocities of the trajectories is randomly assigned from Maxwell-Boltzmann distribution. In this thesis, we study the RTIL system using this isoconfigurational ensemble method in order to find a indicator of dynamic heterogeneity. In addition, we also study a solvation dynamics in RTILs with the same method as an application of RTIL system.

1.4 Coarse-grained model of RTILs

In order to conduct the simulation study using the isoconfigurational ensemble mentioned in Section 2.2, many trajectories are needed to secure the statistically plausible result. Moreover, it is very difficult to simulate RTILs for a time scale, at which the system fully loses the information of the initial state, in a simulation study because RTILs show a very slower dynamics than normal liquids, especially at a lower temperature. To overcome this limitation of long computational time in RTIL system, we employ a coarse-grained (CG) model of RTILs instead of all-atom model. The CG model is widely used for simulating a large systems, such as proteins,[14] DNAs,[15] and polymers[16] as well as RTILs.

Among the various types of CG models developed by many researchers,[17–21] we adopt a CG model for $EMI^+PF_6^-$ described in Ref 10. This model has the similar liquid structure with the all-atom model, and describes well the glassy dynamics of RTILs, such as subdiffusive behavior, stretched exponential decay of intermediate scattering function, and the violation of Stokes-Einstein relaxation, as the temperature is lowered. On the other hand, because dynamics of CG model is accelerated by simplified molecular structure, overall dynamics of GG model at 350 K is similar with that of all-atom model at 400 K. This model is derived from the united atom model in Ref 22. In this model, cation, EMI^+ is composed of four sites, methyl group is represented by a single unified bead (M1), methylene group and methyl group in ethyl group by two unified bead (E1, M3), and 8 atoms in imidazolium ring by a single unified bead (T1), respectivley. (see Figure 1.1) Anion, PF_6^-, is also represented by a single unified bead. For cations, in-

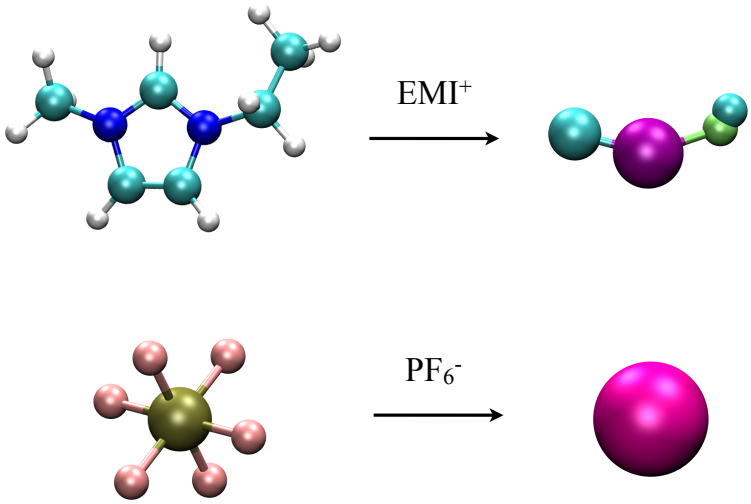

Figure 1.1: Coarse-graining scheme of $EMI^+PF_6^-$

tramolecular interactions are ignored, so that the intramolecular structure of cation is maintained rigid during the simulation. Site-site intermolecular interaction potential is employed by the sum of Lennard-Jones potential and Coulomb interaction

$$U_{ij}(r_{ij}) = 4\epsilon_{ij}\left[\left(\frac{\sigma_{ij}}{r_{ij}}\right)^{12} - \left(\frac{\sigma_{ij}}{r_{ij}}\right)^{6}\right] + \frac{q_i q_j}{4\pi\epsilon_0 r_{ij}} \tag{1.1}$$

where r_{ij} is the distance between site and ϵ_0 is the vacuum permittivity. Lorentz-Berthelot combination rulse, $\sigma_{ij} = \frac{\sigma_{ii}+\sigma_{jj}}{2}$ and $\epsilon_{ij} = \sqrt{\epsilon_{ii}\epsilon_{jj}}$, are used for pairs of different site. LJ parameters and partial charges of our

Table 1.1: Lennard-Jones parameters, partial charge and mass for coarse-grained model of $EMI^+PF_6^-$.

site	σ_{ii} ($\mathring{A}$)	ϵ_{ii} (kJ/mol)	q_i (e)	mass (amu)
M1	3.905	0.7333	0.3160	15.04092
T1	4.800	1.5000	0.3680	67.08860
E1	3.800	4.9430	0.2400	14.03298
M3	3.800	0.7540	0.0760	15.04092
PF_6^-	5.600	1.6680	-1.0000	144.9744

model are listed in Table 1.1 In this thesis, we conduct molecular dynamics simulation of the large number of trajectories in IC ensemble for various conditions, different temperature and excitation energy, with the CG model of RTILs, so that the total number of trajectories are hundreds of thousands. The CG model will enable us to reduce the high computational cost and save the time spent on this study.

1.5 Introduction to solvation dynamics

In this section, we first briefly review solvation dynamics. The model system of the solute and the notation describing solvation dynamics in this thesis will be introduced in the second part of this section.

Solvation dynamics refers to the response of dipolar solvent molecules after an instantaneous change of charge distribution of the solute. Due to the Coulomb interaction between solvent and solute molecules, dipolar solvent molecules reorganize their structure to minimize the total energy of the system. In particular, solvation dynamics in RTILs is significantly different from that in typical polar solvent. In the latter, it has a static electric dipole moment because of the rigidity of molecular structure. In RTILs, cation and anion are mobile and the distance between the ions is variable. Therefore, the solvation structure of RTILs would be different from those of typical solvent. In addition, the mechanism of solvation dynamics is also quite different. While dipole-dipole interaction plays a dominant role and solvent response to the changed charge distribution is mostly induced by the reorientation of molecules in normal solvent, ion-dipole interaction is most dominant and translational motion of the individual ions and collective motions of the constituent ions is the main solvent response in RTILs. These properties of RTILs can affect chemical reactions involving change of the charge distribution, such as charge transfer or electron transfer reaction.

The solvation dymamics is commonly studied by the time-resolved fluorescence spectroscopy on polar probe molecules in a solvent.[23–26] In an experiment using this method, the charge distribution of probe molecules

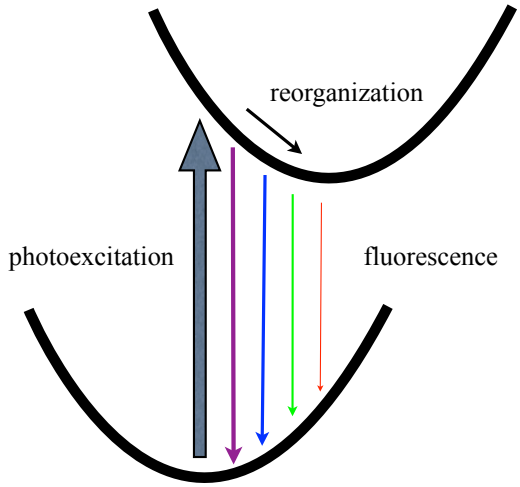

Figure 1.2: Schematic diagram of solvation dynamics

is suddenly altered by photoexcitation with a laser pulse. In response, solvent molecules surrounding the probe proceed reorganizing to a new energy minimum state for newly created charge distribution with time as described schemetically in Figure 1.2. According to this procedure, time evolution of fluorescence spectrum is shifted to the red after the photoexcitation of probe as the solvent molecules are rearranged. The normalized spectral shift, so called Stokes-shift function, can be obtained by extracting the peak frequency of time-dependent fluorescence spectrum, which is defined as

$$S(t) = \frac{\overline{\nu(t)} - \overline{\nu(\infty)}}{\overline{\nu(0)} - \overline{\nu(\infty)}} \tag{1.2}$$

where $\overline{\nu(0)}$, $\overline{\nu(t)}$ and $\overline{\nu(\infty)}$ is the peak frequencies of the time-dependent fluorescence spectrum at time 0, t, and ∞, respectively. In the past decade, many researchers investigated the extensive studies of solvation dynamics of RTILs. One of the interesting features of solvation dynamics in RTILs is the fact that not only their solvation process is extremely slow and time scale of slow relaxation is broadly distributed in time from picosecond to nanosecond, but also relaxation process is biphasic. The simulation studies related to biphasic relaxation are also investigated,[27] which implies that the ultrafast subpicosecond initial relaxation is attributed to an inertial translational motions of Cl^- ion, especially in EMI^+Cl^-, and long time nonexponential decay results from diffusive motion of ions. In spite of many efforts to understand solvation dynamics, various factors which can affect dynamics in solvation process have not yet been fully established. With this respect, we study excitation-energy dependence of solvation dynamics *via* molecular dynamics simulation in Chapter 3

Now, we briefly introduce the model system of the solute and notation used in this thesis. The model of solute in our study is originally proposed in Ref. 28. This is a model system composed of two atoms. The electronic state of the solute is assumed to be nonpolarizable and have two state, a and b. The total energy of the system including the solvent and the solute is defined as E_i $(= a,\ b)$ for a given configuration. The energy difference between the solute electronic states a and b is also defined as

$$\Delta E_{a\to b} \equiv E_b - E_a, \tag{1.3}$$

The two states are assumed to be degenerate in energy *in vacuo* so that $\langle \Delta E_{a\to b}\rangle_a \equiv \langle \Delta E_{a\to b}\rangle$ means the solvation-induced shift of the Frank-

Condon (FC) energy related with the $a \to b$ transition, where $\langle \cdots \rangle_a$ denotes an equilibrium ensemble average in the presence of the solute charge, or the state a. Detailed information for charge distribution of solute will be introduced in Section 3.2.

Time correlation function of a fluctuation of $\Delta E_{a\to b}$, $C(t)$, usually describes the dynamic properties of equilibrium solvation dynamics in the presence of solute state a. The normalized form is defined as

$$C_{a/b}(t) \equiv \frac{\langle \delta\Delta E_{a\to b}(t)\delta\Delta E_{a\to b}(0)\rangle}{\langle (\delta\Delta E_{a\to b}(0))^2\rangle}, \tag{1.4}$$

where $\delta\Delta E_{a\to b}$ is the deviation of $\Delta E_{a\to b}$ from the equilibrium ensemble average $\langle \Delta E_{a\to b}\rangle$. We also define the normalized Stokes-shift functions mentioned above in simulation study as

$$S_{a/b}(t) \equiv \frac{\overline{\Delta E_{a\to b}(t)} - \overline{\Delta E_{a\to b}(\infty)}}{\overline{\Delta E_{a\to b}(0)} - \overline{\Delta E_{a\to b}(\infty)}}, \tag{1.5}$$

where $\overline{\Delta E_{a\to b}(t)}$ denotes the nonequilibrium ensemble average with the $a \to b$ transition at time t after an instantaneous change of solute charge state from b to a at $t = 0$. Note that the initial configuration for calculating $S_{a/b}(t)$ is equilibrated at the b state.

Finally, the solvation frequency, ω_{S} is defined as

$$\omega_{\mathrm{S}} \equiv \Big(\frac{\langle (\delta\Delta \dot{E}_{a\to b})^2\rangle}{\langle (\delta\Delta E_{a\to b})^2\rangle} \Big)^{1/2} \tag{1.6}$$

using the generalized Langevin equation (GLE).[27] $\langle \delta\Delta E_{a\to b})^2\rangle$ and $\langle (\delta\Delta \dot{E}_{a\to b})^2\rangle$ denote the mean-squared fluctuation of $\Delta E_{a\to b}$ and time derivative of $\langle \delta\Delta E_{a\to b})^2\rangle$, respectively. According to the GLE, $C(t)$ can be represented as $\exp[-\omega_{\mathrm{S}}^2 t^2/2]$

in the short time limit, which indicates that ω_{S} describes an initial relaxation of $C_{a/b}(t)$. In Chapter 3, we show the result of dynamic properties of solvation dynamics defined here.

Chapter 2

Dynamic propensity as an indicator of heterogeneity in room-temperature ionic liquids

2.1 introduction

Room-temperature ionic liquids (RTILs) are molten organic salts made of bulky cations and non-coordinating anions.[29,30] Numerous combinations of cations and anions can be designed to have superior physicochemical properties necessary in various applications. For example, nonvolatility and high thermal stability make RTILs a promising alternative to volatile organic solvents or electrolytes in applications for fuel cells,[31] solar cells,[32] and supercapacitor devices.[33] However, higher viscosity of RTILs compared with conventional volatile solvents may deteriorate the performance of ionic liquid-based electrolytes. Viscosity of RTILs varies in a wide range, as we choose different ionic species or add other solvent molecules.[34] It also increases abruptly as the temperature is lowered, signaling the presence of a

glass transition.[35] Due to strong interactions between ions, RTILs exhibit viscous dynamics even at room temperatures, which is strikingly different from normal liquids. This aspect has provoked intense theoretical interest as well as practical issues.

Viscous dynamics in RTILs have been studied theoretically through molecular dynamics simulations by many researchers.[10,22,27,28,36–47] Solvation and rotational dynamics of the solute are found to be described by the nonexponential relaxation in accordance with the experimental results.[23–26,48–57] Translational dynamics of the ions are characterized with the nonexponential structural relaxation, subdiffusive behavior, violation of the Stokes-Einstein relation, and the decoupling phenomena. These phenomena appear clearly as the temperature is lowered.[10]

As a matter of fact, the aforementioned phenomena in the translational dynamics have been observed previously in various models of supercooled liquids,[58–64] where the Coulomb interactions are absent. It is quite interesting that such dynamic features seem to be universal and independent of the types of molecular interactions present in viscous liquids when approaching the glass transition. These phenomena can be understood as arising from the dynamic correlation in the spatio-temporal trajectories of supercooled liquids,[65,66] dubbed dynamic heterogeneity, and it manifests itself as the coexistence of mobile and immobile regions in supercooled liquids. The dynamic heterogeneity also yields the coupling behavior of exchange and persistence times as verified earlier.[10,59]

Although understanding the link between structure and dynamics has been a central question in supercooled liquids and been investigated by many different researchers using various tools,[67] it still remains an open

question to identify the exact mechanism of the development of the dynamic correlation. For example, mechanisms based on purely fluctuation-dominated dynamics as well as those emphasizing dominant influence of the structure have been proposed. To elucidate a possible structural origin of the resulting dynamics, a concept of dynamic propensity has been proposed recently as a measure of an individual particle's movement in a two-dimensional model of supercooled liquids.[11–13] Statistical distributions and spatial patterns of the dynamic propensity have been investigated previously.[68–70] It is observed that the distribution of the dynamic propensity markedly deviates from a Gaussian behavior, displaying a fat tail at high propensities in a supercooled regime. Since the dynamic propensity may encode structural information related to dynamic heterogeneity, it has attracted much attention recently, in particular, regarding to its predictability of the long time dynamics.[68–70]

As mentioned above, dynamics of RTILs at low temperatures are phenomenologically similar to those of supercooled liquids, reflecting the presence of the dynamic heterogeneity. In order to further investigate the dynamical nature of RTILs, we examine statistical properties of the dynamic propensity and discuss nature of the intermittent motions of ions at low temperatures by monitoring how the dynamic propensity reflects heterogeneous dynamics in RTILs. We believe this work is the first application of the concept of dynamic propensity to complex molecular liquids such as RTILs. To connect the dynamic propensity and actual dynamics, we define mobility for each ion, describing dynamic heterogeneity in a single run starting from the same initial positions. We find that the dynamic propensity has weak correlation with individual particle's movement. Instead, spatial patterns

of mobile and immobile regions have correlations with the dynamic propensity patterns, and these collective dynamical fluctuations have a non-local structural origin.

This chapter is organized as follows: In Sec. 2.2, we briefly introduce the dynamic propensity in the isoconfigurational ensemble. A coarse-grained model of an RTIL and simulation methods are summarized in Sec. 2.3. In Sec. 2.4, we analyze of the dynamic propensity and investigate its correlation with the mobility. Finally, we conclude in Sec. 2.5.

2.2 Isoconfigurational ensemble and dynamic propensity

In this section, we briefly introduce IC ensemble as already mentioned in Section 1.3 and dynamic propensity, which have been employed to examine the heterogeneity of various supercooled liquid systems.[11–13,68–73] An equilibrium configuration of molecules in a liquid can be achieved with numerous different sets of momenta following the Maxwell-Boltzmann (MB) distribution in phase space. Such a subset of the equilibrium ensemble defines the IC ensemble, whose the members have the same configuration but different momenta. When we employ the IC ensemble for calculating physical properties by using the ensemble average, variations in the initial momenta are averaged out. Thus, dynamical quantities for each constituent particle in the IC ensemble would provide a clue to structural influence on the resultant dynamics, especially in glass forming liquids where significant movements occur sporadically. With this respect, the dynamic propensity p_i of the i-th particle is introduced to investigate dynamic heterogeneity,

and it represents individual particle's tendency to move for a given configuration,[11–13] defined as

$$p_i \equiv \langle |\mathbf{r}_i(t^*) - \mathbf{r}_i(0)|^2 \rangle_{\mathrm{IC}}, \tag{2.1}$$

where $\langle \cdots \rangle_{\mathrm{IC}}$ denotes the average over the IC ensemble for a given initial configuration. The time interval t^* has been usually chosen on the order of τ_α, which is the structural relaxation time determined from the characteristic time scale of the self-intermediate scattering function $F_s(q_0, t) \equiv \langle \exp[i\mathbf{q_0} \cdot \{\mathbf{r}(t) - \mathbf{r}(0)\}] \rangle$, such that $F_s(q_0, \tau_\alpha) = 1/e$. Here, $\langle \cdots \rangle$ denotes the average over particles and equilibrium ensembles and q_0 represents the wavevector corresponding to the first peak position of the static structure factor for all molecular species.

Previously, Harrowell and coworkers have shown that dynamic propensity does not have a direct relation with several local structural quantities or the potential energy.[12,74] Rather, spatial distributions of the dynamic propensity turns out to be correlated with the Debye-Waller factor, and agrees with an actual resultant dynamics over a large length scale.[12] Appignanesi and coworkers have shown that the dynamic propensity closely reflects the structural constraints of the system at an initial configuration as long as the timescale is not much larger than the relaxation timescale.[69–72] In this study, we set the time interval t^* to be $1.5\tau_\alpha$ as done in the previous studies.[13] Discussions on the use of different values of the time scale will be made later.

Table 2.1: Structural relaxation time τ_α for the cations(+) and anions(-) at various temperatures T. τ_α and T are in unit of ps and K, respectively.

T	τ_α(+)	τ_α(-)
350	1960	4840
400	262	538
475	48.2	80.8
600	11.1	14.9
800	3.4	3.9

2.3 Model description and simulation methods

To achieve good statistics necessary for computing the dynamic propensity at low temperatures, it is convenient to introduce a coarse-grained model of an RTIL. We employ a simple model of the RTIL, 1-ethyl-3-methylimidazolium hexafluorophosphate ($EMI^+PF_6^-$), which has been introduced in Section 1.4 The system consists of 512 pairs of cations and anions confined in a cubic box of length 55.0 Å, where the density is set to be 1.31 g/cm^3. For the Lennard-Jones parameters and partial charges of the coarse-grained atom are listed in Table 1.1

Molecular dynamics (MD) simulations were conducted in the NVT ensemble through the use of the DL_POLY simulation package. We have used the Nosé-Hoover thermostat and employed the Verlet-leapfrog algorithm with a time step of 2 fs for numerical integrations. Long-range electrostatic interactions were computed with the Ewald summation method.

In preparation for obtaining the dynamic propensity, we produce equi-

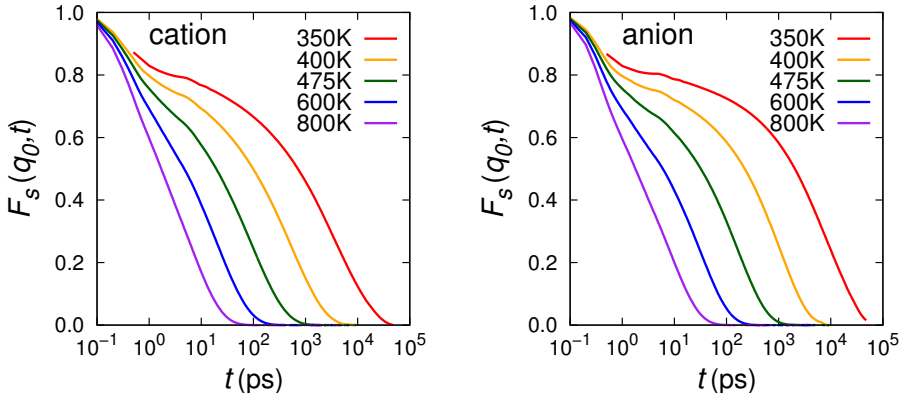

Figure 2.1: Self-intermediate scattering fuction $F_s(q_0, t)$ for cations (left) and anions (right) at various temperatures.

librium configurations at various temperatures and determine the time interval t^* defined in Eq. 2.1. Initially, we generate five different equilibrium configurations at $T = 800\,\mathrm{K}$, of which subsequent ones were separated by 2 ns interval, long enough to make them statistically uncorrelated from each other. When equilibrating the system at lower temperatures, an initial configuration is taken as one of the equilibrium configurations at the nearest higher temperature. In this manner, we obtain five equilibrium configurations at each temperature of $T = 600\,\mathrm{K}$, $475\,\mathrm{K}$, $400\,\mathrm{K}$, and $350\,\mathrm{K}$. Then, we perform MD simulations to calculate the self-intermediate scattering function $F_s(q_0, t)$, and obtain the structural relaxation time τ_α for each temperature. Figure 2.1 shows the intermediate scattering function $F_s(q_0, t)$ averaged over five independent trajectories at different temperatures, where q_0 is set to be $1.24\,\mathrm{\AA}^{-1}$. We set the time interval t^* to be $1.5\tau_\alpha$ as done in

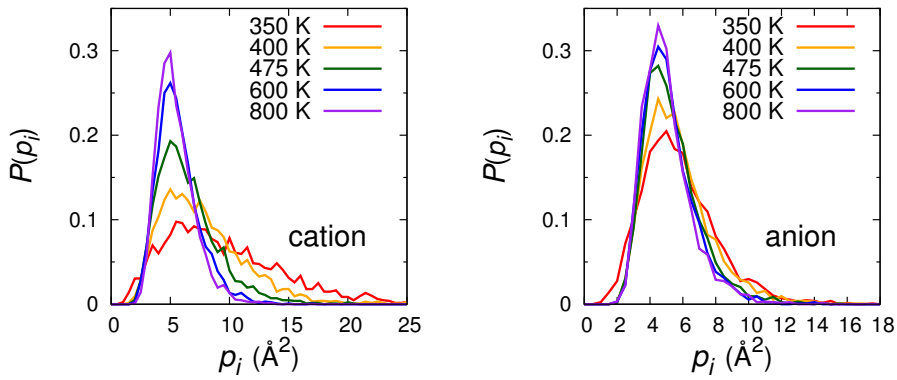

Figure 2.2: Distributions of propensity p_i averaged over five configurations for the cations (left) and anions (right) at various temperatures.

the previous studies.[13] τ_α's for the cations and anions at five temperatures are compiled in Table 2.1.

When calculating the dynamic propensity, we produce 200 trajectories at a given configuration with newly assigned momenta, following the MB distribution at each temperature. The dynamic propensity is determined to be the average of squared displacements of each ion during t^*.

2.4 Results and discussions

2.4.1 Distributions of dynamic propensity

We have calculated distributions of the dynamic propensity for the cations and anions separately, by taking the averages over the five independent initial configurations. In Fig. 2.2, the probability distributions $P(p_i)$ of propen-

sities for the cations and anions are presented at five different temperatures. At 800 K, the highest temperature studied, the ions move around relatively freely due to thermal fluctuations. Thus, each ion is in a statistically identical environment during t^*, which results in the Gaussian distribution of $P(p_i)$ according to the central limit theorem. On the other hand, as the temperature is lowered, $P(p_i)$ becomes broad and asymmetric, especially for the case of cations. This suggests that the motions of each ion must have been influenced by different local structures, since the effect of initial momenta in the IC ensemble has already been averaged out. In other words, ions with low propensity are initially in a very restrictive environment, while ions with high propensity are free of such restrictions. This indicates that the distribution of propensity should give information on the development of the dynamic heterogeneity as the temperature is lowered.

Now we compare the results of the cations and anions. At low temperatures, developments of fat tails in the distribution with decreasing temperature are more prominent in cations than in anions. It implies that environments surrounding the anions are relatively homogeneous than those surrounding the cations. We note that τ_α for the anion is about 2.5 times larger than that of the cation as presented in Sec. 2.3. During the structural relaxation time of the anions, the cations locally arranged around an anion may fully relax, so that the effect of dynamic constraint is averaged out. Moreover, due to the spherical geometry, the anions take part in the local relaxation dynamics less actively than cations. Therefore, dynamics of the cations make more important contributions to the dynamic heterogeneity of our RTIL system.

Sufficiently sampled IC ensemble would reflect the system at equilib-

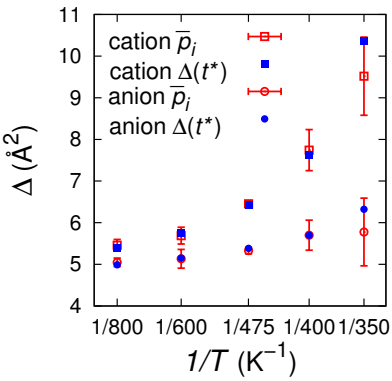

Figure 2.3: Mean square displacement $\Delta(t^*)$ and $\overline{p_i}$ for cations and anions at various temperature. Error bars are estimated from the standard deviations of $\overline{p_i}$ for five configurations.

rium. If this is the case, $\overline{p_i}$, the averaged propensity over the given ionic species, should be the same as the value of the mean squared displacement (MSD) at time t^*, $\Delta(t^*) \equiv \langle N^{-1} \sum_i |\mathbf{r}_i(t^*) - \mathbf{r}_i(0)|^2 \rangle$. Because the system is in the diffusive regime at t^*, the mean squared displacement linearly increases with time such that $\Delta(t^*) \approx 6Dt^*$, where D denotes the diffusion coefficient. In the case of normal liquids, the Stokes-Einstein (SE) relation is satisfied and $D\tau_\alpha$ is constant, independent of the temperature. If this is the case, by recalling that $t^* = 1.5\tau_\alpha$ in this work, it can be shown that $\overline{p_i} \approx \Delta(t^*) \approx 9D\tau_\alpha$, regardless of the temperature. However, Fig. 2.3 shows that both $\overline{p_i}$ and $\Delta(t^*)$ increase as the temperature is lowered, and this indicates the violation of the SE relation. It also shows that the dynamics of the cation violates the SE relation more dramatically than that of the

anion. This is consistent with the previous observation of the dominant role played by the cations in heterogeneous dynamics.

2.4.2 Statistics in the isoconfigurational ensemble

We consider the fluctuations among different trajectories in the IC ensemble. In order to do that, we define σ_i as the standard deviation of squared displacements of i-th ion,

$$\sigma_i = \left[\langle \Delta {r_i}^4 \rangle_{\mathrm{IC}} - \langle \Delta {r_i}^2 \rangle_{\mathrm{IC}}^2\right]^{1/2}. \tag{2.2}$$

We first focus on the correlation between the propensity and standard deviation. Scatter plots of σ_i and p_i for the cations and anions at 350 K and 800 K are shown in Fig. 2.4. First of all, we notice that at 350 K, σ_i's show a positive deviation from the result that would be obtained by assuming three-dimensional random walk, $\sigma_i = (2/3)^{1/2} p_i$, represented by a solid line both for cations and anions. At 800 K, however, the data are consistent with the random walk result. These observations suggest that the dynamics of the RTIL at 350 K do not follow simple random walk motions, and instead, there are additional dynamical fluctuations contributing to intermittent, large displacements of ions. At both temperatures, ions (especially cations) with a high propensity generally show large σ_i. This implies that ions with a high propensity does not necessarily mean that they all exhibit large displacements in a given single trajectory.

Based on these observations, it seems important to look at the distributions of the propensity of individual ions, and further to probe possible correlation with other dynamical quantities of ions. Thus, we consider dis-

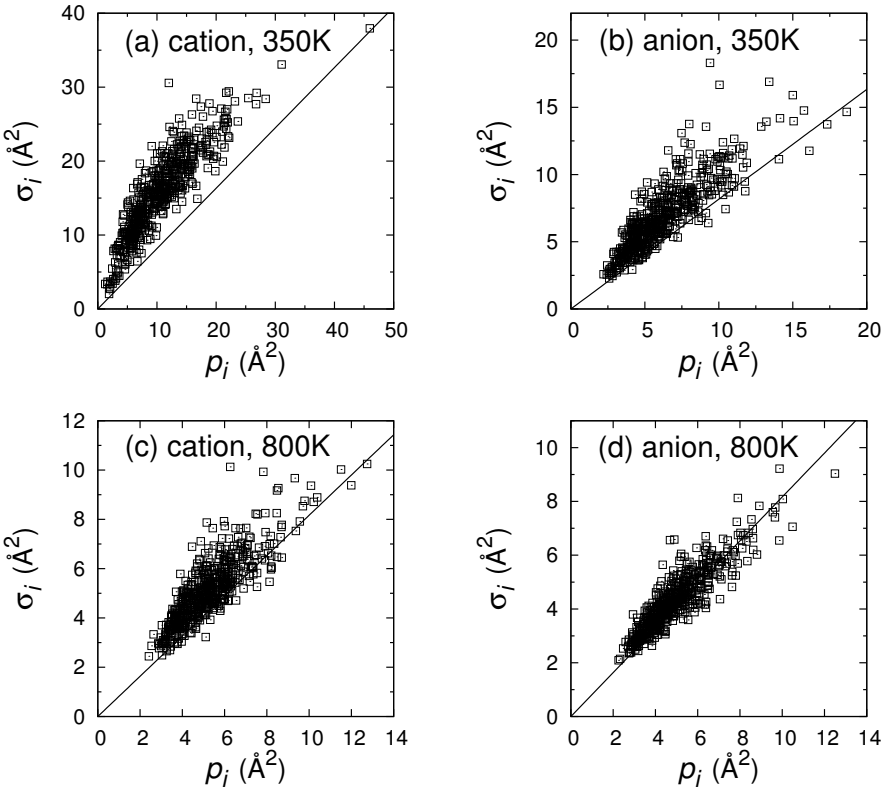

Figure 2.4: The correlations between the propensity p_i and the standard deviation of the propensity σ_i for the (a) cations at 350 K, (b) anions at 350 K, (c) cations at 800 K, and (d) anions at 800 K. The solid line indicates the 3D random walk result, $\sigma_i = (2/3)^{1/2} p_i$.

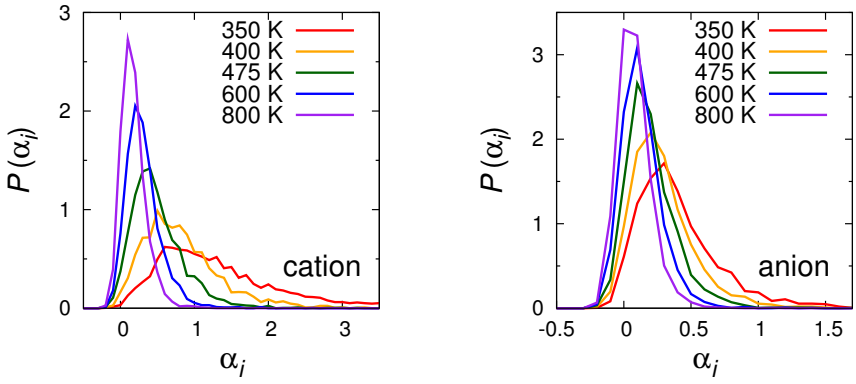

Figure 2.5: Distributions of the non-Gaussian parameter α_i averaged over five configurations for cations (left) and anions (right) at various temperatures.

tributions of the displacements of the i-th ion during t^*, denoted by $f_i(\Delta r)$, to further describe the statistics in the IC ensemble. Then, the propensity p_i corresponds to the second moment of $f_i(\Delta r)$. Note that the distribution $f_i(\Delta r)$ is obtained from different trajectories of the same i-th ion starting from the same initial configuration, and not a quantity averaged over different ions. In order to characterize the distribution $f_i(\Delta r)$, the non-Gaussian parameter α_i is defined to be

$$\alpha_i \equiv \frac{3\langle \Delta r_i^4 \rangle_{\mathrm{IC}}}{5\langle \Delta r_i^2 \rangle_{\mathrm{IC}}^2} - 1. \tag{2.3}$$

In Fig. 2.5, the distributions of α_i for the cations and anions are displayed at five temperatures. At 800 K, the distribution is narrow and its mean value almost vanishes. As the temperature is lowered, the distribu-

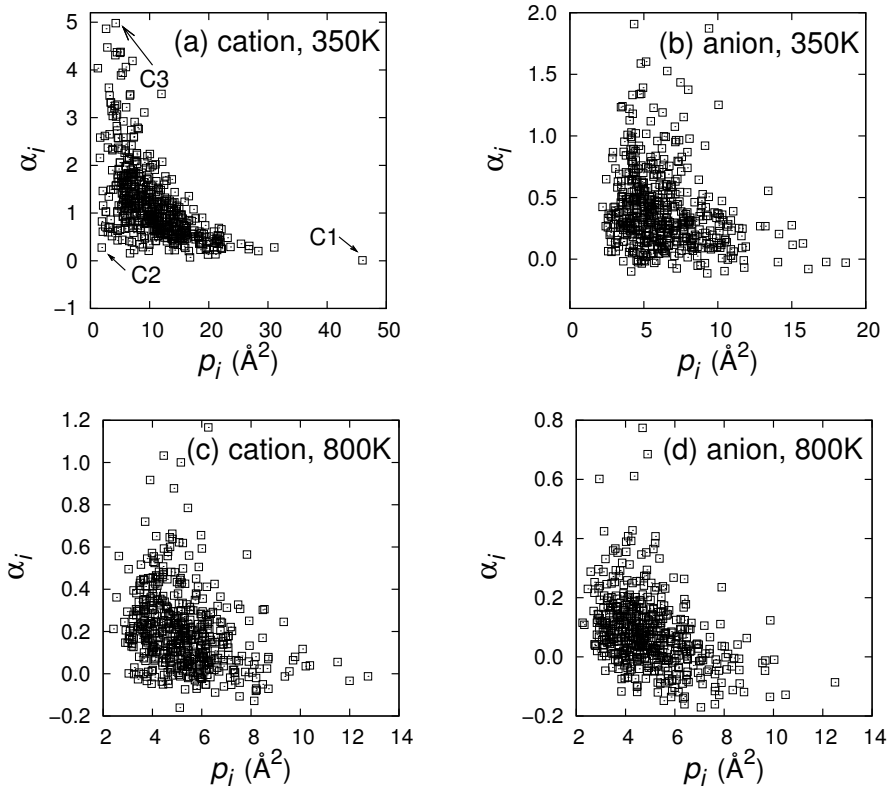

Figure 2.6: The correlations between the propensity p_i and the non-Gaussian parameter α_i for the (a) cations at 350 K, (b) anions at 350 K, (c) cations at 800 K, and (d) anions at 800 K.

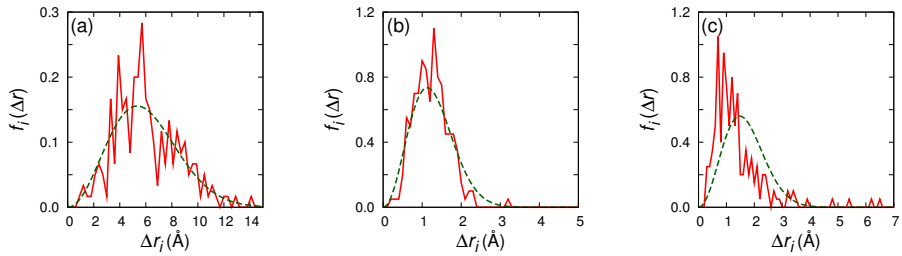

Figure 2.7: $f_i(\Delta r)$ in the IC ensemble are shown for three representative cations of (a) C1, (b) C2, and (c) C3 chosen in Fig. 2.6 at 350 K. The solid line indicates the original distributions over 200 runs and the dashed line indicates the Gaussian distribution, constructed with the average and standard deviation of the original one.

tions shift to the right with broadening, indicating the increase of non-Gaussianity in the IC ensemble. The deviation of σ_i from the random walk result shown in Fig. 2.4 is also due to the non-Gaussian character of the IC ensemble at a low temperature.

In the scatter plots of α_i and p_i shown in Fig. 2.6, the cations with high p_i tend to have rather small values of α_i. On the other hand, for small values of $p_i (\lesssim 10\,\text{Å}^2)$, α_i exhibits a wide variation: α_i is mostly less than 2, but about 14% of the cations exhibit larger values of α_i. This behavior indicates that there is a wide variation in the behavior of individual ion's motions in RTILs. In order to further characterize the statistics of intermittent dynamics of cations, three representative cations marked by C1, C2, and C3 in Fig. 2.6 are selected. Values of p_i for C1, C2, and C3 are found to be $46.0\,\text{Å}^2$, $1.91\,\text{Å}^2$, and $4.27\,\text{Å}^2$, respectively, and α_i are found to be 0.00873,

0.276, and 4.98. In Fig. 2.7(a)-(c), $f_i(\Delta r)$ for C1-3 are displayed in the solid lines. For reference, we show Gaussian distributions, denoted by dashed lines, which are constructed by using p_i and σ_i, as mean and standard deviation, respectively, for each case. As inferred from the corresponding values of α_i, $f_i(\Delta r)$ for C1 and C2 are almost consistent with $g_i(\Delta r)$, while $f_i(\Delta r)$ for C3 markedly deviates from $g_i(\Delta r)$.

This analysis allows us to infer that different dynamical behaviors would be possible for individual ions. For example, C1 and C2 exhibit Gaussian statistics peaked at high and low propensity value, respectively. This indicates that there are some ions whose dynamics are closely dominated by the initial configuration, mobile for C1 and immobile for C2, up to the time scale of t^*. On the other hand, for the case of C3, the propensity is low but the non-Gaussian parameter is quite large, and the distribution shows clear deviation from the Gaussian. Thus, C3-like cations would have undergone small displacement motions in most of the trajectories, with some exceptions of large displacements in a few trajectories. This is a manifestation of intermittent dynamics arising due to the fluctuation-dominated dynamics of the RTIL.[10]

2.4.3 Propensity vs. Mobility

In this section, we study how the spatial heterogeneity of dynamic propensity reflects the actual dynamics starting from the same initial configurations. The dynamics of the ions are described by another particle-based quantity, named the mobility in this study. We examine possible correlations and spatial overlaps between the dynamic propensity and mobility obtained from a single run.

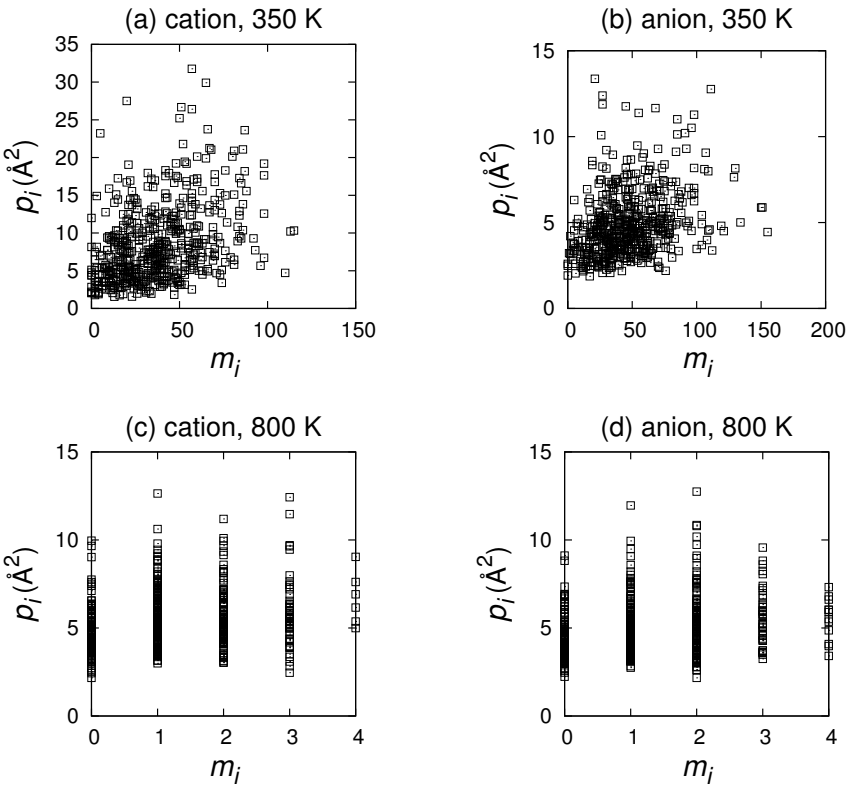

Figure 2.8: The correlation plots for the propensity p_i versus the mobility m_i for the (a) cations at 350 K, (b) anions at 350 K, (c) cations at 800 K, and (d) anions at 800 K.

To quantify the motions of each ion in the trajectory, we define the mobility by counting the local excitation events. We regard the displacement of an ion by a distance larger than a threshold distance d as an excitation,[10,63] where d is chosen to be $\sqrt{5}$ Å in this study. To be specific, if the position $\mathbf{r}_i$ for the center of mass of i-th ion follows $|\mathbf{r}_i(t_1) - \mathbf{r}_i(0)| = d$, $|\mathbf{r}_i(t_2) - \mathbf{r}_i(t_1)| = d$, etc., then t_1, $t_2, \cdots$ are identified as the instances of the excitation events. Other choices of d corresponding to the length scale of subdiffusive motion do not change our results in terms of identifying mobile and immobile ions. Effects of the cut off distance d on the average time interval between subsequent excitations were considered in a previous study.[10] We note that a larger value of d should give more sparse excitations, resulting in the difficulty in the analysis.

The mobility of the i-th ion, denoted by m_i, is defined as the number of excitation events occurred during the time interval t^*. We set t^* to be $1.5\tau_\alpha$, the same as the time interval for calculating the dynamic propensity in the previous section. The heterogeneous dynamics of the RTIL is described by distributions of m_i, which specifies the dynamic state of an ion being mobile or immobile.

In Fig. 2.8, we present correlation plots of the dynamic propensity p_i and mobility m_i for cations and anions at 350 K and 800 K. Overall, the correlation plot develop a "fan-like" structure. At 350 K, m_i and p_i exhibit weak correlations for cations and anions in Fig. 2.8(a) and (b), respectively. On the other hand, at 800 K, p_i seems independent of m_i in Fig. 2.8(c) and (d). Note that at 800 K m_i's are quite small because of short relaxation time.

The correlation between p_i and m_i can be quantified conveniently with

the linear correlation coefficient Q, which is defined to be

$$Q \equiv \frac{\overline{\delta p_i \delta m_i}}{\sqrt{\overline{\delta p_i}^2}\sqrt{\overline{\delta m_i}^2}}, \tag{2.4}$$

where δp_i and δm_i are $p_i - \overline{p_i}$ and $m_i - \overline{m_i}$, respectively, and overlines denote averaging over the same ionic species. The correlation coefficients Q for cations and anions are found to be 0.43 and 0.35 at 350 K, respectively, while 0.24 and 0.26 at 800 K, which indicates there is rather a weak correlation between the propensity and mobility overall. This tells that dynamic propensity itself is not predictive of the mobility of individual ions.

Although there is an overall, weak correlation between the propensity and mobility, once we focus on the low mobility-low propensity region, rather a strong correlation between the two is observed. To be specific, when the propensity is below 5 Å^2, we see few data corresponding to the mobility over 60 in Fig. 2.8(a). Low propensities reflect structural constraints imposed on the initial configuration, resulting immobile region in the subsequent dynamics. On the other hand, ions of higher propensities cover a wide range of mobility. This is consistent with with the results of Sec. 2.4.2, that is, the standard deviation of the displacement for an ion calculated in the IC ensemble increases with p_i, and a high p_i for an ion provides little information about the motions of the ion in a single run.

In fact, connections between high propensity and mobility regions have been developed previously in the case of atomic liquid systems.[69–72] In atomic liquid systems, it has been shown that glassy systems relax through sequences of intermittent, large scale excitation events, and when these happen, patterns of the dynamic propensity lose their correlations. Physically, this would correspond to transitions between different metabasins of liquid

configurations. When this event happens, new patterns of dynamic propensity develops, utilizing more mobile regions for the next relaxation events. While there is a whole distribution of timescales, it is known that the typical timescales of such events are on the order of the metabasin lifetime, shorter than the structural relaxation time.

Thus, one can imagine the following scenario. In the heterogeneous dynamics of the RTIL, the system loses the pattern of initial constraints with widely distributed time scales. In the region where the initial constraints decorrelates fast, the actual dynamics becomes rather independent of the initial structure, while in the region where they decorrelate slowly, the correlation between the mobility and propensity is preserved. Note that this decorrelation pattern would depend upon the time scale used, which is chosen as $t^* = 1.5\tau_\alpha$ in this study. Thus, it seems plausible to correlate different types of dynamical behaviors of cations, classified as C1–C3 in Sec. 2.4.2 to different cases of decorrelation patterns of dynamic propensities, which is certainly subject to more thorough investigation.

Although one needs to check if the above scenario really applies to more complex liquid systems such as RTILs studied in this work, our results seem to be consistent with this picture, and it could possibly be the reason why we find rather weak correlation between the propensity and mobility when they are calculated at the time scale $t^* = 1.5\tau_\alpha$. Certainly it would be interesting to see how the correlation between the two quantities vary when the timescale becomes shorter.

Though we have not observed distinct correlations between p_i and m_i of all ions, we expect that they may develop spatial correlations in their distribution patterns. We thus present overlap of spatial distributions of

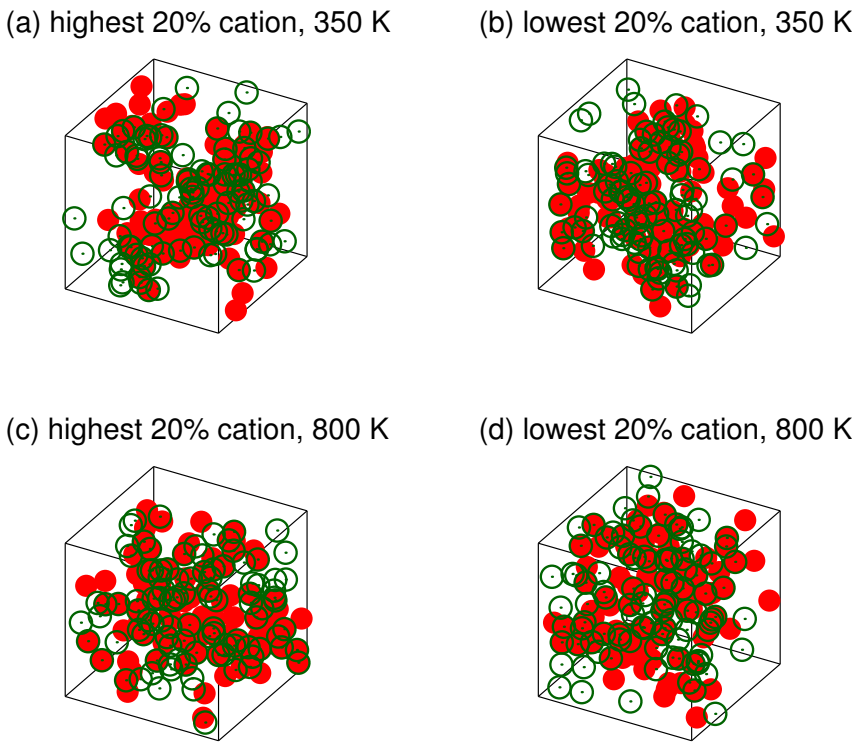

Figure 2.9: Spatial overlap between propensity (filled red circles) and mobility (empty green circles) for the cases of (a) highest 20 % cations at 350 K, (b) lowest 20% cations at 350 K, (c) highest 20 % cations at 800 K, (d) lowest 20 % cations at 800 K.

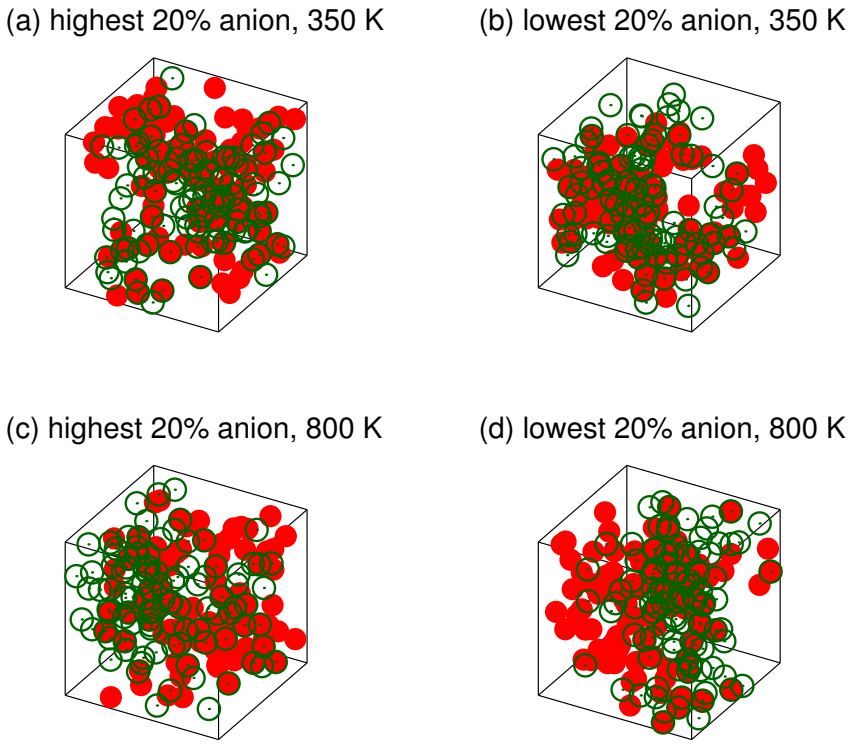

Figure 2.10: Spatial overlap between propensity (filled red circles) and mobility (empty green circles) for the cases of (a) highest 20 % anions at 350 K, (b) lowest 20 % anions at 350 K, (c) highest 20 % anions at 800 K, and (d) lowest 20 % anions at 800 K.

ions with higher (or lower) p_i together with those with higher (or lower) m_i for an initial configuration at 350 K and 800 K, both for cations in Fig. 2.9 and for anions in Fig. 2.10, respectively. In these figures, filled red circles represent ions with highest (or lowest) 20% of propensities, while empty green circles represent those with highest (or lowest) 20% of mobilities, respectively. The radii of all particles are set to be same. It is clear that at 350 K ions with high propensities are distributed forming clusters. Moreover, ions with high mobility indeed show strong correlation with those with high propensity. This is not the case at a higher temperature of 800 K.

2.5 Conclusions

We investigated the dynamic propensity in a model RTIL system via molecular dynamics simulations in this chapter. It turns out that our RTIL model system also exhibits heterogeneous distributions of the dynamic propensity at room temperatures. We find that as the temperature is lowered, the dynamic propensity develops broad distributions, which indicates the significance of dynamic heterogeneity in the relaxation dynamics of the system. We also find that cations play more dominant roles in the development of the dynamic heterogeneity than anions.

We tried to address an important issue on the dynamic propensity: how it reflects heterogeneous dynamics in RTILs. By observing the statistical quantities in the isoconfigurational ensemble, we observed that the dynamic propensity do not show strong correlation with the mobility at the timescale used in this study. This finding is certainly consistent with previous results obtained in the atomic liquid systems.[69–72] It would be an important and

intriguing issue to probe how the correlation between the two quantities vary as the timescale changes.

While we do not find the strong correlation between the propensity and the mobility based on individual ions, spatial patterns of the high (or low) propensity ions seem to be correlated with those of mobile (or immobile) regions, respectively. Although more detailed analysis of spatial patterns of mobility/propensity distributions may be necessary, our observation implies that any structural aspects relevant to spatial heterogeneity of the dynamics should involve length scales larger than inter-ion distances, which is in agreement with a previous study.[68] Along this line, we will perform further studies regarding the length scale of the heterogeneity and the possibility of the long-ranged structural properties.

Chapter 3

Excitation-energy dependence of solvation dynamics in room-temperature ionic liquids

3.1 Introduction

Room-temperature ionic liquids (RTILs) consisting of bulky asymmetric organic cations and anions have attracted broad interest because of their unique properties, such as high chemical, electrical, and thermal stabilities, low vapor pressure, and large electrochemical window.[1,75,76] It has also been suggested that RTILs are a new type of solvents or electrolytes that can replace conventional aqueous and organic solvents in a wide range of applications in chemistry and electrochemistry. Due to their strong Coulomb interaction and disordered molecular structure, RTILs can exist in a liquid state at room temperature, but have very high viscosity, which induces distinctive properties in dynamics.[10,77,78]

Among others, solvation dynamics in RTILs have received a great deal

of experimental[23–25,48,53,56,79–83] and theoretical[27,28,39–41,44–47,52,84–89] attention in recent years. Their relaxation over a wide range of timescales spanning hundreds of femtoseconds to tens and hundreds of nanoseconds reveals RTILs' unique dynamic character. In the case of imidazolium-based ILs, for example, solvation dynamics show biphasic relaxation—ultrafast subpicosecond dynamics, followed by a very slow non-exponential decay.

Interestingly, solvation free energy profiles of RTILs were found to be approximately parabolic, indicating that the Marcus free energy relationship is generally valid for electron transfer reactions in RTIL environments.[90–92] From this perspective of nearly harmonic potentials, nonequilibrium solvent relaxation is closely related to equilibrium solvent fluctuation dynamics.[27]

Recently, a considerable experimental effort has been focused on excitation-wavelength dependence of solvation dynamics in RTILs.[93–96] Related dependence of steady-state emission spectra on the excitation energy, so-called red-edge effect (REE), has also been examined for RTILs both experimentally[26,97,98] and theoretically.[42,43,99] Time-resolved spectroscopy measurements indicate that solvation dynamics vary with the excitation wavelength.[93–96] In some experiments, solvation dynamics were found to become faster with increasing excitation energy[93,96] but in some others, the opposite trend was obtained.[94,96] Thus while it is generally accepted that heterogeneity of RTILs is responsible for excitation-wavelength dependent solvation dynamics, there is a clear need for further analysis to better understand this interesting phenomenon.

In most of the previous simulation studies, initial configurations needed for solvent relaxation subsequent to the electronic excitation of the probe solute were chosen randomly from configurations equilibrated to the probe

in the ground electronic state. The resulting initial configurations are characterized by a broad distribution in energies and thus do not allow a detailed study of the dependence of nonequilibrium solvation dynamics on the excitation energy. In this article, we circumvent this difficulty by considering multiple sets of initial configurations, each set with an extremely narrow distribution of excitation energy with a different mean. The comparison of solvent relaxation obtained with different sets of initial configurations enables a direct analysis of its dependence on the excitation energy. To gain insight into the effects of structural heterogeneities on solvation dynamics, we also investigate the time evolution of variance of emission energies using the isoconfigurational ensemble method. As a prototypical RTIL, we consider 1-ethyl-3-methylimidazolium hexafluorophosphate ($EMI^+PF_6^-$) using a coarse-grained model description and compared with aprotic acetonitrile.

The rest of this chapter is organized as follows: Model descriptions and simulation methods are briefly explained in Section 3.2. In Section 3.3, we analyze the Stokes-shift function and the steady-state emission spectrum, focusing on their dependence on the excitation wavelength. Comparison of nonequilibrium and equilibrium solvation dynamics is also made there. Concluding remarks are offered in Section 3.4

3.2 Model description and simulation methods

The simulation box comprises a single diatomic solute immersed either in 256 pairs of EMI^+ and PF_6^-, or in 512 molecules of CH_3CN. Two constituent atoms of the rigid solute molecule are separated by 0.55 nm and interact with the solvent molecules through the Lennard-Jones and Coulomb

potential. The atomic mass of each atom of the solute is 154.64 amu and LJ parameters are $\sigma = 0.4$ nm and $\epsilon = 0.83$ kJmol^{-1}. We considered two types of solute charge distributions: a neutral pair (NP) with no charges and an ionic pair (IP) with charges $q = \pm\ 0.6364e$, which yield a dipole moment of 16.8 D (e = elementary charge). For $EMI^+PF_6^-$, we used the coarse-grained description of Ref. 10, in which EMI^+ are modeled as four sites connected through rigid bonds and PF_6^- is described as a united atom. For acetonitrile, the all-atom description of Ref. 100 was employed.

All simulations were performed in the canonical (NVT) ensemble with Nosé-Hoover thermostat using the GROMACS packages.[101] The box size and the temperature employed were, respectively, $L = 4.364$ nm and $T = 350$ K for $EMI^+PF_6^-$ and 3.555 nm and 300 K for acetonitrile. Periodic, cubic boundary condition was applied and long-range electrostatic interactions were computed with the Particle-mesh Ewald summation method. The trajectories were integrated via the Verlet algorithm using a time step of 2 fs with data saved every 20 fs. For equilibrium simulations, 5 different trajectories were considered for both $EMI^+PF_6^-$ and CH_3CN. For each trajectory, the production run was 25 ns long for $EMI^+PF_6^-$ and 30 ns long for CH_3CN.

The Franck-Condon (FC) energy between solute electronic states a and b with different charge distributions

$$\Delta E_{a\to b} \equiv E_b - E_a\ , \tag{3.1}$$

is widely used as a collective molecular variable[102] in simulation studies to make direct contact with time-resolved spectroscopy measurements. Nonequilibrium simulations are usually performed by instantaneously switch-

ing the solute electronic state from b to a (i.e., FC excitation) in the presence of a solvent configuration equilibrated to b and by averaging the ensuing time evolution of $\Delta E_{a\to b}$ over an ensemble of initial configurations. Thus the preparation of a reliable set of initial configurations is crucial for a nonequilibrium study. Since our main goal is to scrutinize the excitation-wavelength-dependence of solvation dynamics, we consdiered different excitation energies and their corresponding sets of initial configurations. Specifically, we selected 8 different excitation energies by shifting $\Delta E_{a\to b}$ from its equilibrium value to lower energies, i.e., $\Delta E_{a\to b} = \langle \Delta E_{a\to b} \rangle - \Delta E_{\rm shift}$, where $\Delta E_{\rm shift}$ measures the degree of red shift of the excitation wavelength. Here $\langle \Delta E_{a\to b} \rangle$ ($\equiv \langle \Delta E_{a\to b} \rangle_a$) is the equilibrium absorption energy and $\langle \cdots \rangle_a$ denotes an equilibrium ensemble average in the presence of the solute in state a (= NP or IP). In the present study, we considered $\Delta E_{\rm shift}$ values of 0, 2.5, 5, 7.5, 10, 15, 30 45 kcal/mol.

For each of the $\Delta E_{\rm shift}$ values, we selected 400 configurations from equilibrium configurations in such a way that they are at least 50 ps apart from one another and satisfy $|\Delta E_{a\to b} - (\langle \Delta E_{a\to b} \rangle - \Delta E_{\rm shift})| \le \sigma_{\rm E}$ with $\sigma_{\rm E} = k_{\rm B}T/300$. It is well known that if the $\Delta E_{\rm shift}$ value exceeds the energy fluctuations at equilibrium, sampling using the standard Boltzmann distribution becomes unreliable due to limited MD statistics. We thus introduced solute charges intermediate between NP and IP à la free energy perturbation method[103] to generate reliable $\Delta E_{a\to b}$ distributions centered at differing absorption energies. Three intermediate charge states were considered: QP with $q = \pm 0.1591e$, HP with $\pm$ $0.3182e$, and TP with $\pm$ $0.4773e$. For illustration, the probability distributions of $\Delta E_{\rm IP\to NP}$ obtained with these intermediate charges as well as with NP and IP are shown in Figure 3.1.

It is worthwhile to note that the distributions obtained with the NP and IP states hardly overlap, clearly exposing the difficulty with the standard Boltzmann sampling when ΔE_{shift} is large. The distributions obtained with QP, HP and TP ensure that a broad region of $\Delta E_{\text{IP}\to\text{NP}}$ from its equilibrium value, $\langle\Delta E_{\text{IP}\to\text{NP}}\rangle$, to lower energies and thus a wide range of red shifts in the excitation energy are covered reasonably well statistically.

Once a set of 400 configurations was generated for each of the 8 different values of ΔE_{shift} using equilibrium trajectories obtained with NP, QP, HP, TP and IP solutes, we constructed 50 different sets of velocities according to the Maxwell distribution and generated a velocity or isoconfigurational ensemble[11,77] for each of the 400 configurations. Different members of an isoconfigurational ensemble have different sets of initial momenta assigned to the molecules/ions but they all share exactly the same configuration of initial positions for the molecules/ions. This enables to separate variances arising from initial structure and initial dynamics of the solute-solvent system and analyze their respective influence on subsequent relaxation. All nonequilibrium simulations were conducted for 1 ns in $EMI^+PF_6^-$ and for 200 ps in acetonitrile. A total of *20,000 different microstates* in phase space were employed to compute averages of nonequilibrium relaxation *for given initial excitation wavelength*, i.e., a given $\Delta E_{\text{IP}\to\text{NP}}$ or $\Delta E_{\text{NP}\to\text{IP}}$ value.

3.3 Result and discussion

3.3.1 Equilibrium and nonequilibrium property

Simulation results for the time-correlation function, $C_{a/b}(t)$, of solvent fluctuations at equilibrium, and dynamic Stokes shift function, $S_{a/b}(t)$, of the

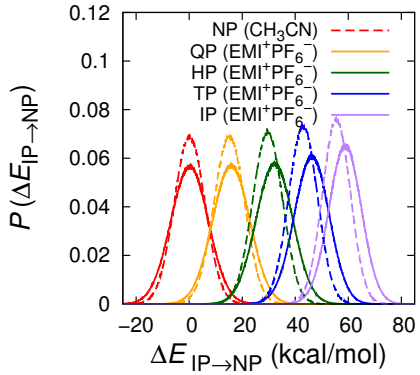

Figure 3.1: Distribution function of $\Delta E_{\mathrm{IP}\to\mathrm{NP}}$ of equilibrium simulation for five solute state, NP, QP, HP, TP, and IP, in $\mathrm{EMI}^{+}\mathrm{PF}_6{}^{-}$ (solid line) and acetonitrile (dashed line).

nonequilibrium FC energy relaxation defined as

$$C_{a/b}(t) \equiv \frac{\langle \delta\Delta E_{a\to b}(t)\delta\Delta E_{a\to b}(0)\rangle}{\langle(\delta\Delta E_{a\to b}(0))^2\rangle} \ , \tag{3.2}$$

and

$$S_{a/b}(t) \equiv \frac{\overline{\Delta E_{a\to b}(t)} - \overline{\Delta E_{a\to b}(\infty)}}{\overline{\Delta E_{a\to b}(0)} - \overline{\Delta E_{a\to b}(\infty)}} \ , \tag{3.3}$$

are presented in Figure 3.2. In Eqs. 3.2 and 3.3, $\delta\Delta E_{a\to b}$ is the deviation of $\Delta E_{a\to b}$ from the equilibrium ensemble average $\langle\Delta E_{a\to b}\rangle$, and $\overline{\Delta E_{a\to b}(t)}$ denotes the nonequilibrium ensemble average of the $a \to b$ transition at time t after an instantaneous change of solute charge state from b to a at $t = 0$. As mentioned above, an ensemble of 20,000 trajectories is used to calculate $S_{a/b}(t)$ in our study.

We first consider the results in the left panels, where $C_{a/b}(t)$ and $S_{a/b}(t)$

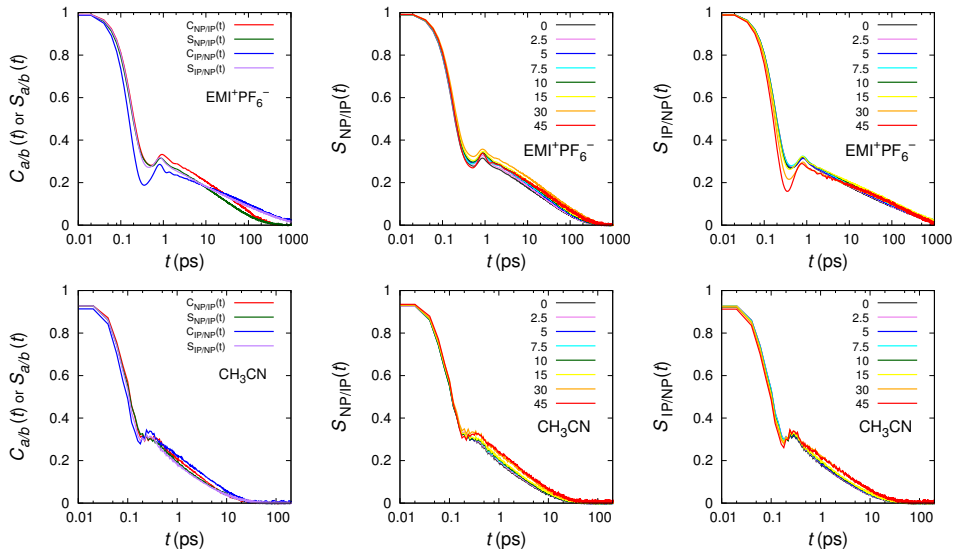

Figure 3.2: Left: Comparison of the normalized time-correlation function, $C_{a/b}(t)$, and the Stokes-shift function, $S_{a/b}(t)$, for NP/IP and IP/NP cases in $EMI^+PF_6^-$ (top) and acetonitrile (bottom). Middle: $S_{a/b}(t)$ for NP/IP case in $EMI^+PF_6^-$ (top) and acetonitrile (bottom) with various ΔE_{shift}, 0, 2.5, 5, 7.5, 10, 15, 30 45 kcal/mol. Right: $S_{a/b}(t)$ for IP/NP case with the same red-shift as the middle panels.

(with $\Delta E_{\text{shift}} = 0$) are compared. Overall, our results compare reasonably well with those of an earlier study[27] though the all-atom and united-atom descriptions employed there for $EMI^+PF_6^-$ are quite different from our coarse-grained model description. Both $C_{a/b}(t)$ and $S_{a/b}(t)$ are characterized by biphasic relaxation, i.e., ultrafast subpicosecond initial relaxation and a very slow nonexponential decay. The former and the latter

are attributed, respectively, to hindered translational and diffusive motions of RTIL ions.[27,28,45–47,52,84,87] We notice that $C_{a/b}(t)$ and $S_{a/b}(t)$ in the presence of the solute in the same ground state exhibit similar long-time behaviors in $EMI^+PF_6^-$. This confirms the conjecture made in Ref. 27 that equilibrium and nonequilibrium solvation dynamics, if they occur under similar RTIL environments, will share similar temporal behaviors. By contrast, the results for $C_{a/b}(t)$ and $S_{a/b}(t)$ in acetonitrile are almost superimposable regardless of their solute electronic states, revealing that linear response holds very well in this solvent.

Properties of equilibrium solvation dynamics we obtained are summarized in Table 3.1. Our result for $\langle \Delta E_{a\to b} \rangle$ for $EMI^+PF_6^-$ is 58.7 kcal/mol, which is smaller than that in Ref. 27 obtained with the IP solute charges of ± 1.0 e. This is as expected because $\langle \Delta E_{a\to b} \rangle$, which gauges the solute-solvent electrostatic interaction, is nearly proportional to the magnitude of the diatomic solute charges. This trend was also observed in Ref. 40.

Table 3.1: Equilibrium properties of solvation dynamics¶

solvent	a/b	$\langle \Delta E_{a\to b} \rangle$	$\langle (\delta \Delta E_{a\to b})^2 \rangle$	$\langle (\delta \Delta \dot{E}_{a\to b})^2 \rangle$	ω_S
$EMI^+PF_6^-$	NP/IP	-0.141	55.1	2431	6.6
	IP/NP	58.7	38.2	2443	8.0
CH_3CN	NP/IP	-0.165	34.0	12119	18.9
	IP/NP	55.6	27.8	11971	20.7

¶ Energy unit: kcal/mol, time unit: ps

The solvent frequency, $\omega_{\rm S} \equiv \left(\frac{\langle (\delta \Delta \dot{E}_{a\to b})^2 \rangle}{\langle (\delta \Delta E_{a\to b})^2 \rangle} \right)^{1/2}$, which measures the inertial relaxation of $C_{a/b}(t)$, increases as the solute ground state is changed from NP to IP. This behavior arises primarily from $\langle (\delta \Delta E_{a\to b})^2 \rangle$ that becomes reduced in the presence of a charged solute, compared to a neutral solute. The enhancement in solvent structure near the solute induced by strong solute-solvent Coulomb interactions ("electrostriction") and accompanying increase in structural rigidity make solvent fluctuations difficult, thereby lowering $\langle (\delta \Delta E_{a\to b})^2 \rangle$.[22] Because $\langle (\delta \Delta \dot{E}_{a\to b})^2 \rangle$ is similar for IP and NP, a decrease in $\langle (\delta \Delta E_{a\to b})^2 \rangle$ yields an increase in $\omega_{\rm S}$. Therefore, the short time relaxation of $C_{a/b}(t)$ becomes accelerated with increasing solute charge distribution.

The middle and right panels of Figure 3.2 show $S_{a/b}(t)$ with different $\Delta E_{\rm shift}$. Though there are discernible differences, the overall relaxation behavior of $S_{a/b}(t)$ does not vary too much with $\Delta E_{\rm shift}$. This appears to be in agreement with experimental results. Similar to $C_{a/b}(t)$, $S_{a/b}(t)$ show biphasic relaxation irrespective of initial excitation energies.

Though not huge, we quantitate the influence of $\Delta E_{\rm shift}$ on solvent relaxation by fitting $C_{a/b}(t)$ and $S_{a/b}(t)$ as a combination of a Gaussian and a stretched exponential function[52]

$$f(t) = f_{\rm G} \exp(-\omega_{\rm G}^2 t^2/2) + (1 - f_{\rm G}) \exp\{-(t/\tau)^\beta\} \ . \tag{3.4}$$

The fitting parameters of $C_{a/b}(t)$ and $S_{a/b}(t)$ are compiled in Table 3.2 and Table 3.3. There are several noteworthy aspects. First, as $\Delta E_{\rm shift}$ increases, the short time relaxation of $S_{a/b}(t)$ becomes faster (i.e., its $\omega_{\rm G}$ increases) in the IP/NP case but becomes slower (and its $\omega_{\rm G}$ decreases) in the NP/IP case. This is closely related to the observation made above

Table 3.2: Fitting parameters of $S_{a/b}(t)$ with various ΔE_{shift} and $C_{a/b}(t)$ in $EMI^+PF_6^-$. ‖

solvent	a/b	ΔE_{shift}	f_{G}	ω_{G}	τ	β
$EMI^+PF_6^-$	NP/IP	0	0.65	8.26	22.9	0.49
		2.5	0.64	8.19	23.5	0.49
		5	0.63	8.15	25.9	0.50
		7.5	0.64	8.05	30.6	0.52
		10	0.65	7.92	32.1	0.53
		15	0.64	7.82	32.9	0.52
		30	0.64	7.57	46.0	0.53
		45	0.68	7.88	45.6	0.55
		$C_{a/b}(t)$	0.70	7.65	49.2	0.65
	IP/NP	0	0.64	7.66	35.7	0.33
		2.5	0.65	7.73	40.3	0.34
		5	0.66	7.82	46.6	0.35
		7.5	0.66	7.84	50.7	0.36
		10	0.66	8.05	61.6	0.36
		15	0.68	8.17	88.0	0.39
		30	0.74	8.41	116.1	0.47
		45	0.76	9.32	137.9	0.53
		$C_{a/b}(t)$	0.71	9.80	75.9	0.38

‖ The numbers in the third column indicate ΔE_{shift} for $S_{a/b}(t)$ and the last rows of each solute state indicate fitting parameters of $C_{a/b}(t)$. The energy unit is kcal/mol and the time unit is ps

Table 3.3: Fitting parameters of $S_{a/b}(t)$ with various $\Delta E_{\mathrm{shift}}$ and $C_{a/b}(t)$ in acetonitrile.

solvent	a/b	$\Delta E_{\mathrm{shift}}$	f_{G}	ω_{G}	τ	β
CH_3CN	NP/IP	0	0.51	13.9	1.20	0.44
		2.5	0.51	13.9	1.28	0.45
		5	0.52	14.2	1.46	0.46
		7.5	0.52	14.3	1.47	0.45
		10	0.52	14.6	1.54	0.46
		15	0.52	14.2	1.63	0.46
		30	0.52	14.5	2.06	0.50
		45	0.56	15.8	2.74	0.54
		$C_{a/b}(t)$	0.57	14.7	1.95	0.54
	IP/NP	0	0.51	14.4	1.13	0.43
		2.5	0.50	14.5	1.14	0.43
		5	0.51	14.8	1.22	0.43
		7.5	0.52	14.9	1.34	0.44
		10	0.52	15.5	1.35	0.44
		15	0.53	15.7	1.44	0.44
		30	0.56	17.0	2.32	0.48
		45	0.57	17.4	2.34	0.46
		$C_{a/b}(t)$	0.58	17.8	2.65	0.52

that the initial relaxation of $C_{a/b}(t)$ becomes faster as the solute charge increases. Specifically, in the case of $S_{\mathrm{IP/NP}}(t)$, an increase in $\Delta E_{\mathrm{shift}}$ makes the initial configurations more "IP-like" environments and thus accelerates the solvent relaxation, while it is the opposite in the case of $S_{\mathrm{NP/IP}}(t)$. Since increase in $\Delta E_{\mathrm{shift}}$ weakens the perturbation to the system caused by the initial excitation, linear response is better followed with increasing $\Delta E_{\mathrm{shift}}$. One consequence of this is that ω_{G} of $S_{a/b}(t)$ becomes closer to that of $C_{a/b}(t)$ with increasing $\Delta E_{\mathrm{shift}}$ for both the IP/NP and NP/IP cases.

The long time relaxation of $S_{a/b}(t)$, gauged by τ and β, also generally converges to that of $C_{a/b}(t)$ as $\Delta E_{\mathrm{shift}}$ increases. As above, this is ascribed to the decreasing perturbation with increasing $\Delta E_{\mathrm{shift}}$. Interestingly, $S_{a/b}(t)$ with $\Delta E_{\mathrm{shift}} = 0$ tends to relax faster than $C_{a/b}(t)$ at long times regardless of the solute charge states. As such, the long-time relaxation of $S_{a/b}(t)$ becomes slower as $\Delta E_{\mathrm{shift}}$ and thus the excitation wavelength increase for both the NP/IP and IP/NP cases. This is different from short-time dynamics considered above, which show differing trends of ω_{G} for the IP/NP and NP/IP cases. We note that the long-time relaxation of both $S_{a/b}(t)$ and $C_{a/b}(t)$ in acetonitrile shows a non-exponential behavior ($\beta \approx 0.5$) according to our simulations, whereas an exponential decay was obtained with a coarse-grained model in Ref. 52 We ascribe this difference to two factors: slower diffusion in the all-atom model than in the coarse-grained model at the same temperature and the partial charges of hydrogen atoms of the methyl groups that tend to enhance short-range specific interactions.

3.3.2 Variance analysis: configuration vs. velocity

We turn to the effects of the initial configuration and velocity distributions on nonequilibrium solvent relaxation. To estimate their respective influence, we consider three different variances[68] of $\Delta E_{a\to b}(t)$, $\Delta_{\text{total}}(t)$, $\Delta_{\text{vel}}(t)$, and $\Delta_{\text{con}}(t)$ defined as

$$\begin{aligned}
\Delta_{\text{total}}(t) &= \langle \Delta E_{a\to b}(t)^2 \rangle_{x,p} - \langle \Delta E_{a\to b}(t) \rangle_{x,p}^2 \ ; \\
\Delta_{\text{vel}}(t) &= \langle \langle \Delta E_{a\to b}(t)^2 \rangle_p - \langle \Delta E_{a\to b}(t) \rangle_p^2 \ \rangle_x \ ; \\
\Delta_{\text{con}}(t) &= \langle \langle \Delta E_{a\to b}(t) \rangle_p^2 \rangle_x - \langle \Delta E_{a\to b}(t) \rangle_{x,p}^2 \\
&= \Delta_{\text{total}}(t) - \Delta_{\text{vel}}(t) \ ,
\end{aligned} \tag{3.5}$$

where $\langle \cdots \rangle_p$ and $\langle \cdots \rangle_x$ indicate a nonequilibrium average over the isoconfigurational ensemble of 50 trajectories (i.e., average over different initial velocities for a given configuration) and over 400 different initial configurations, respectively. Δ_{total} is the total variance of $\Delta E_{a\to b}(t)$ determined with the full ensemble (i.e., 20,000 trajectories), while Δ_{vel} arising from differing initial velocity assignments measures the influence of the initial velocity distribution on later dynamics. The contribution from the distribution of initial configurations, Δ_{con}, is determined as the difference of Δ_{total} and Δ_{vel}. The results of the three variances with different ΔE_{shift} are presented in Figure 3.3, Figure 3.4 and Figure 3.5 for $EMI^+PF_6^-$.

In all cases we studied, Δ_{total} in Figure 3.3 start with 0 because the $\Delta E_{a\to b}(t)$ value at $t = 0$ is identical for all 20,000 trajectories for a given excitation energy. Their increase in time reveals that the solvent relaxation progresses in different pathways. In many cases, Δ_{total} reaches its maxi-

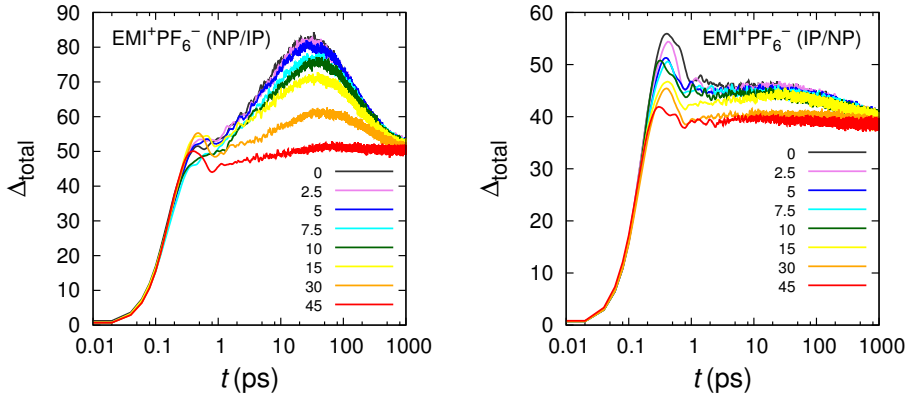

Figure 3.3: The variance of total trajectories, Δ_{total}, of $\Delta E_{a\to b}(t)$ in nonequilibrium simulations for NP/IP (left) and IP/NP (right) cases with various ΔE_{shift}, 0, 2.5, 5, 7.5, 10, 15, 30, and 45 kcal/mol, in $\text{EMI}^{+}\text{PF}_6{}^{-}$.

mum in less than ~ 1 ps, indicating that relaxation pathways become most heterogeneous in the same time scale as ultrafast subpicosecond decay in $\text{EMI}^{+}\text{PF}_6{}^{-}$. By contrast, several cases of NP/IP relaxation are characterized by a maximum in Δ_{total} located near 20 ps (see below). However, even in these cases, Δ_{total} has either a local minimum or a shoulder structure near 1 ps. As expected, Δ_{total} converges to the equilibrium value of $\langle(\delta\Delta E_{a\to b})^2\rangle$ at long times (see Table 3.1) regardless of the initial conditions. This demonstrates explicitly that nonequilibrium fluctuations in the long time limit become equivalent to equilibrium fluctuations.

A further insight can be gained by decomposing Δ_{total} into Δ_{vel} and Δ_{con}. The results in Figure 3.4 show that Δ_{con} reaches its maximum value at $t \lesssim 1$ ps. This maximum, responsible for the main peak or shoulder

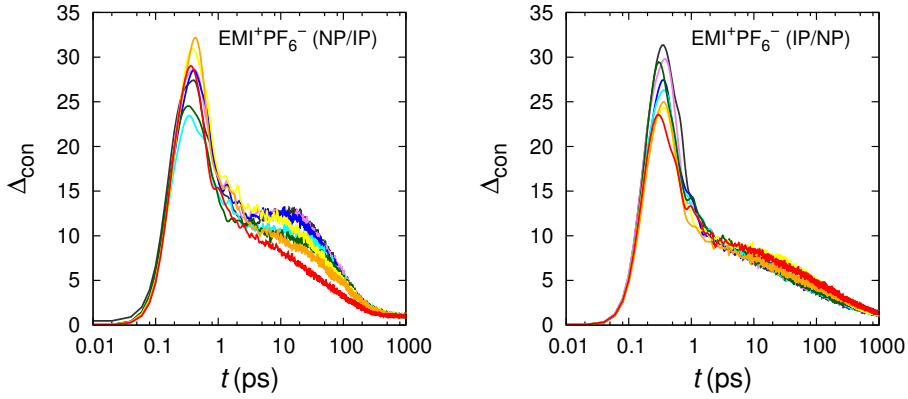

Figure 3.4: Δ_{con} of $\Delta E_{a\to b}(t)$ in nonequilibrium simulations for NP/IP (left) and IP/NP (right) cases with various $\Delta E_{\mathrm{shift}}$, 0, 2.5, 5, 7.5, 10, 15, 30, and 45 kcal/mol, in $\mathrm{EMI}^{+}\mathrm{PF}_6{}^{-}$.

structure observed in Δ_{total}, shows that Δ_{con} is the major contributor to Δ_{total} at short times. While Δ_{con} shows a rather steep decrease after maximum, Δ_{vel} gradually increases. As a result, Δ_{vel} becomes totally dominant in Δ_{total} at long times. These differing behaviors of Δ_{con} and Δ_{vel} suggest that initial configurations can influence subsequent dynamics only for a short period of time. This is consistent with a previous study of a binary Lennard-Jones liquid system;[69] there it was also found that initial configurations can not predict long time dynamics. One salient aspect of Δ_{vel} is that for $\Delta E_{\mathrm{shift}} \lesssim 30\,\mathrm{kcal/mol}$, it is a non-monotonic function of time with a maximum occurring near $t = 100\,\mathrm{ps}$ in the NP/IP case. This is ascribed to the absence of the solute-solvent Coulomb interactions with the NP solute charge distribution. Specifically, abrupt elimination of the IP-solvent

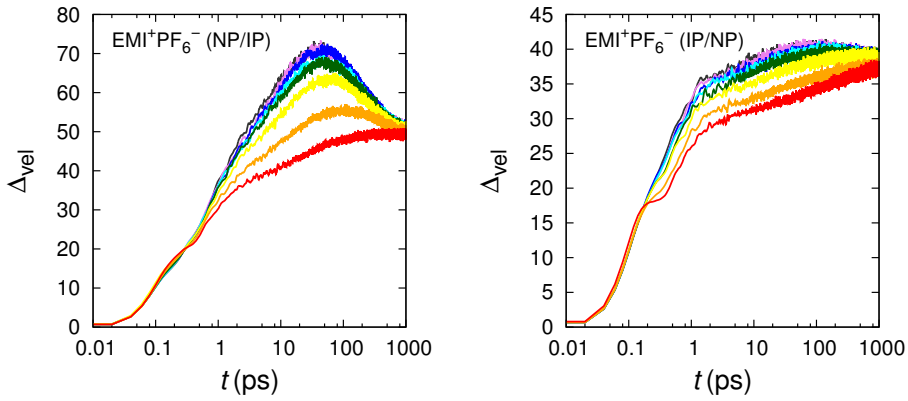

Figure 3.5: Δ_{vel} in nonequilibrium simulations for NP/IP (left) and IP/NP (right) cases with various $\Delta E_{\mathrm{shift}}$, 0, 2.5, 5, 7.5, 10, 15, 30, and 45 kcal/mol, in $\mathrm{EMI}^{+}\mathrm{PF}_6{}^{-}$.

Coulomb interactions with the initial excitation in the NP/IP case subjects solvent ions to a strong nonequilibrium force, which helps the solvent to explore a large "volume" of relaxation pathways, i.e., a large degree of variations in relaxation pathways. As $\Delta E_{\mathrm{shift}}$ increases, the initial solvent environment becomes less "IP-like" and the nonequilibrium force the solvent feels after FC excitation becomes reduced. As a result, the volume of reaction pathways that can be explored and hence Δ_{vel} decrease. The variances have generally lower values with greater $\Delta E_{\mathrm{shift}}$, suggesting that the degree of variations in relaxation pathways becomes smaller as the initial nonequilibrium state is generated closer to the fully relaxed equilibrium state. This means that at given time, the linewidth of the fluorescence emission spectrum decreases as the excitation wavelength increases. It would be

interesting to see if this behavior would be borne out in experiments.

3.3.3 Effect of the solute dipole moment

In this section, we study the influence of solute dipole moment on solvation dynamics by considering the QP and HP charge distributions (see Sec. 3.2 above). The diatomic solute model employed in the present work has been extensively utilized over the past decade [22,27,28,39,40,52,84,85,91] because solvation dynamics in room temperature ionic liquids are well captured through this model. However, since the dipole difference of the IP and NP states used here is somewhat larger than that of typical dye molecules, it is worthwhile to investigate how the dipole difference of the ground and excited states of the probe solute affects its solvation dynamics. To do so, we analyzed $C_{a/b}(t)$ and $S_{a/b}(t)$ for the QP (4.2 D) and HP (8.4 D) solutes that have a smaller dipole moment than the IP (16.8 D) solute. $C_{a/b}(t)$ and $S_{a/b}(t)$ for the QP/NP and HP/NP cases were obtained by eq. (3.2) and eq. (3.3); 10,000 initial configurations selected from those used for the IP/NP and NP/IP cases were employed for $S_{a/b}(t)$ calculations. We note that $C_{a/b}(t)$ for the NP/QP and NP/HP cases are exactly the same as that for the NP/IP case because equilibrium dynamics occur in the presence of the same NP state in all three cases. $S_{a/b}(t)$ for the NP/QP and NP/HQ cases are similar to $S_{a/b}(t)$ for NP/IP with $\Delta E_{\text{shift}} = 45$ and 30 kcal/mol, respectively.

The results for $C_{a/b}(t)$ and $S_{a/b}(t)$ for QP/NP and HP/NP are exhibited in Figure 3.6. For comparison, the results for the IP/NP case are also shown there. Overall solvation dynamics do not vary strongly with the dipole moment of the active state a. Despite some minor differences, especially in

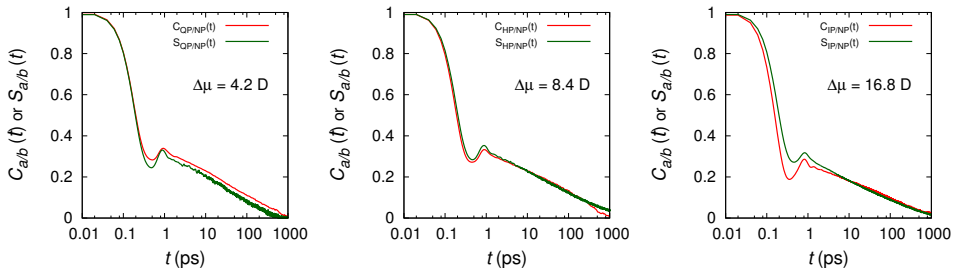

Figure 3.6: Comparison of the normalized time-correlation function, $C_{a/b}(t)$, and the Stokes-shift function, $S_{a/b}(t)$, for QP/NP (left), HP/NP (middle), and IP/NP cases (right) in $EMI^+PF_6^-$.

$C_{a/b}(t)$, all three dipolar states, IP, HP and QP, show very similar relaxation behaviors, including the biphasic character and time scale of $C_{a/b}(t)$ and $S_{a/b}(t)$ dynamics. Furthermore, according to a recent study,[104] a diatomic solute similar to ours captures main features of solvation dynamics of a dye molecule, such as coumarin 153, correctly. These findings indicate that the IP/NP solute system provides a very reasonable framework to study solvation dynamics in RTILs and our analysis based on it is robust.

3.3.4 Steady-state emission spectrum

Finally, we examine the steady-state emission spectrum of the diatomic solute given by[43]

$$I_{a/b}(\Delta E_{\mathrm{em}}) = \int_0^\infty \delta(E_b(t) - E_a(t) - \Delta E_{\mathrm{em}}) \times e^{-t/\tau_{\mathrm{f}}} dt, \qquad (3.6)$$

where τ_{f} is the fluorescence lifetime of the solute and a and b denote its ground and excited states. Since solvent relaxation occurs in the presence

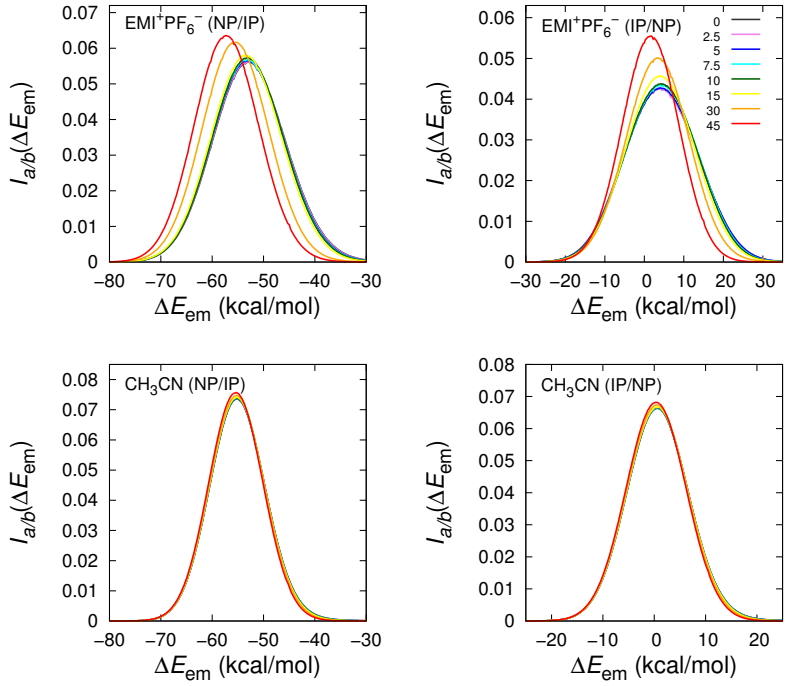

Figure 3.7: The steady-state emission spectra for NP/IP (left) and IP/NP (right) cases in $EMI^+PF_6^-$ (top) and acetonitrile (bottom).

of the solute in state b in Eq. 3.6, solvent dynamics relevant to $I_{a/b}$ are given by $S_{b/a}(t)$.

The results determined with various ΔE_{shift} are displayed in Figure 3.7. As mentioned above, the larger the ΔE_{shift} value, the lower the absorption energy and the closer the initial nonequilibrium FC state to the free energy minimum of the excited state. Each spectrum is obtained by averaging over 20,000 trajectories which have equal excitation energy and area nor-

malized. The lifetime of the solute is arbitrarily chosen as 100 ps, which roughly corresponds to the lifetime of 2-amino-7-nitrofluorene (ANF) probe molecule.[26,43]

The emission spectra show significant dependence on the absorption energy in $EMI^+PF_6^-$ for both NP/IP and IP/NP, whereas they are nearly identical in acetonitrile. Our extensive nonequilibrium simulation study based on a large number of trajectories thus provides convincing evidence for the presence of REE in RTIL systems, in good agreement with Ref. 43.

3.4 Conclusion

In the present chapter, we studied solvation dynamics of a probe solute and related fluorescence spectra in $EMI^+PF_6^-$ with a special focus on the effect of the excitation energy by performing MD simulations with a coarse-grained model description. Despite differences in potential models, our results for overall solvation dynamics share common features with previous studies.[27,52] Specifically, the time correlation function $C_{a/b}(t)$ of solvation energy fluctuations and the time-dependent Stokes shift function $S_{a/b}(t)$ are characterized by two regimes, i.e., ultrafast relaxation followed by a slow decay. These functions show deviations at short times but become nearly congruent at long times in $EMI^+PF_6^-$. By contrast, $C_{a/b}(t)$ and $S_{a/b}(t)$ in acetonitrile obtained with an all-atom potential model show a good agreement in the entire time range we studied.

One of our main findings was that the more the excitation energy is red-shifted, the slower the long time relaxation of $S_{a/b}(t)$ becomes in $EMI^+PF_6^-$. Furthermore, $S_{a/b}(t)$ gradually converges to $C_{a/b}(t)$ as ΔE_{shift}

increases. The solvent frequency ω_G and the time-scale τ, gauging the short time and the long time dynamics, respectively, become closer to those of $C_{a/b}(t)$, complying with the linear response theory. We have also examined the effect of the initial configurations and velocity distributions on the nonequilibrium solvent relaxation by analyzing the variances of 20,000 different trajectories but with the same initial excitation energy. The contribution of the initial configuration to the variance diminishes while that of the initial velocity grows as time evolves. We found that the steady-state emission spectrum varies with the excitation energy in $EMI^+PF_6^-$ due to the slow relaxation of the solvent compared with the fluorescence lifetime of the probe.

One novel aspect of our analysis is that we employed iso-excitation-energy ensembles, i.e., we constructed initial configurations that yield the same excitation energy. This enabled us to examine the dependence of nonequilibrium dynamics and emission spectrum on the excitation energy, in contrast to previous works where the excitation energies are sampled randomly.[27,43,52] In addition, we simulated a large number of trajectories, 20,000 for each ΔE_{shift}, to study nonequlibrium relaxation, adopting the isoconfigurational ensemble approach. This not only yields excellent statistics but also permits analysis of variances of relaxation dynamics arising from initial structure and dynamics. The use of computationally-efficient coarse-grained RTIL model made this analysis possible (the total cumulative simulation time for RTIL was 320 μs). To our knowledge, the present study is the first simulation to carry out excitation-energy-selective nonequilibrium solvation dynamics using the isoconfigurational ensemble method. Moreover, our study demonstrates that using the concept of dy-

namic propensity, the isoconfigurational ensemble method provides useful insight into solvation dynamics in a way similar to prior studies of dynamic heterogeneity of supercooled liquid [11] and RTIL systems. [77]

In the present study, we used the fluorescence lifetime of 100 ps, pertinent to ANF probe molecules. It would be desirable in the future to extend this by considering a range of different solute lifetimes to examine the solute dependence of the emission spectrum and REE. It would be also worthwhile to study the time dependent emission spectra to investigate the time scale at which the REE appears distinctly.

Bibliography

[1] Hallett, J. P.; Welton, T. *Chem. Rev.* **2011**, *111*, 3508.

[2] Wishart, J. F. *Energy Environ. Sci.* **2009**, *2*, 956.

[3] Angell, C. A.; Nagi, K. L.; McKenna, G. B.; McMillan, P. F.; Martin, S. W. *J. Appl. Phys.* **2000**, *88*, 3113.

[4] Ediger, M. D. *Annu. Rev. Phys. Chem.* **2000**, *51*, 99.

[5] Debenedetti, P. G.; Stillinger, F. H. *Nature* **2001**, *410*, 259–267.

[6] Lubchenko, V.; Wolynes, P. G. *Annu. Rev. Phys. Chem.* **2007**, *58*, 235–266.

[7] Berthier, L.; Biroli, G. *Rev. Mod. Phys.* **2011**, *83*, 587–645.

[8] Berthier, L. *Physics* **2011**, *4*, 42.

[9] Stillinger, F. H.; Debenedetti, P. G. *Annu. Rev. Condens. Matter Phys.* **2013**, *4*, 263–285.

[10] Jeong, D.; Choi, M. Y.; Kim, H. J.; Jung, Y. *Phys. Chem. Chem. Phys.* **2010**, *12*, 2001–2010.

[11] Widmer-Cooper, A.; Harrowell, P.; Fynewever, H. *Phys. Rev. Lett.* **2004**, *93*, 135701–4.

[12] Widmer-Cooper, A.; Harrowell, P. *Phys. Rev. Lett.* **2006**, *96*, 185701.

[13] Widmer-Cooper, A.; Harrowell, P. *J. Chem. Phys.* **2007**, *126*, 154503.

[14] Tozzini, V. *Curr. Opin. Struct. Biol.* **2005**, *15*, 144–150.

[15] Maffeo, C.; Ngo, T. T. M.; Ha, T.; Aksimentiev, A. *J. Chem. Theory Comput.* **2014**, *10*, 2891–2896.

[16] Yang, S.; Qu, J. *Phys. Rev. E* **2014**, *90*, 012601.

[17] Wang, Y.; Feng, S.; Voth, G. A. *J. Chem. Theory Comput.* **2009**, *5*, 1091–1098.

[18] Roy, D.; Maroncelli, M. *J. Phys. Chem. B* **2010**, *114*, 12629–12631.

[19] Merlet, C.; Salanne, M.; Rotenberg, B. *J. Phys. Chem. C* **2012**, *116*, 7687–7693.

[20] Wang, Y.-L.; Lyubartsev, A.; Lu, Z.-Y.; Laaksonen, A. *Phys. Chem. Chem. Phys.* **2013**, *15*, 7701–7712.

[21] Salanne, M. *Phys. Chem. Chem. Phys.* **2015**, *17*, 14270–14279.

[22] Shim, Y.; Choi, M. Y.; Kim, H. J. *J. Chem. Phys.* **2005**, *122*, 044510–12.

[23] Karmakar, R.; Samanta, A. *J. Phys. Chem. A* **2002**, *106*, 6670–6675.

[24] Karmakar, R.; Samanta, A. *J. Phys. Chem. A* **2002**, *106*, 4447–4452.

[25] Karmakar, R.; Samanta, A. *J. Phys. Chem. A* **2003**, *107*, 7340–7346.

[26] Samanta, A. *J. Phys. Chem. B* **2006**, *110*, 13704–13716.

[27] Shim, Y.; Choi, M. Y.; Kim, H. J. *J. Chem. Phys.* **2005**, *122*, 044511–12.

[28] Shim, Y.; Duan, J.; Choi, M. Y.; Kim, H. J. *J. Chem. Phys.* **2003**, *119*, 6411–4.

[29] Holbrey, J. D.; Seddon, K. R. *Clean Products Processes* **1999**, *1*, 223.

[30] Wasserscheid, P.; Keim, W. *Angew. Chem. Int. Ed.* **2000**, *39*, 3772.

[31] Noda, A.; Kubo, A. B.; Mitsushima, S.; Hayamizu, K.; Watanabe, M. *J. Phys. Chem. B* **2003**, *107*, 4024.

[32] Wang, P.; Zakeeruddin, S. M.; Moser, J.-E.; Grätzel, M. *J. Phys. Chem. B* **2003**, *107*, 13280.

[33] Tsuda, T.; Hussey, C. L. *Interface* **2007**, *16*, 42.

[34] Wang, J.; Tian, Y.; Zhao, Y.; Zhuo, K. *Green Chemistry* **2003**, *5*, 618.

[35] Ito, N.; Richert, R. *J. Phys. Chem. B* **2007**, *111*, 5016.

[36] Shim, Y.; Jeong, D.; Choi, M. Y.; Kim, H. J. *J. Chem. Phys.* **2006**, *125*, 061102.

[37] Shim, Y.; Jeong, D.; Manjari, S.; Choi, M. Y.; Kim, H. J. *Acc. Chem. Res.* **2007**, *40*, 1130.

[38] Jeong, D.; Shim, Y.; Choi, M. Y.; Kim, H. J. *J. Phys. Chem. B* **2007**, *111*, 4920–4925.

[39] Jeong, D.; Choi, M. Y.; Jung, Y.; Kim, H. J. *J. Chem. Phys.* **2008**, *128*, 174504–8.

[40] Shim, Y.; Kim, H. J. *J. Phys. Chem. B* **2010**, *114*, 10160–10170.

[41] Margulis, C. J. *Mol. Phys.* **2004**, *102*, 829.

[42] Hu, Z.; Margulis, C. J. *J. Phys. Chem. B* **2006**, *110*, 11025–11028.

[43] Hu, Z.; Margulis, C. J. *Proc. Natl. Acad. Sci. U.S.A.* **2006**, *103*, 831–836.

[44] Bhargava, B. L.; Balasubramanian, S. *J. Chem. Phys.* **2005**, *123*, 144505.

[45] Kobrak, M. N.; Znamenskiy, V. *Chem. Phys. Lett.* **2004**, *395*, 127 – 132.

[46] Kobrak, M. N. *J. Chem. Phys.* **2006**, *125*, 064502.

[47] Kobrak, M. N. *J. Chem. Phys.* **2007**, *127*, 184507.

[48] Samanta, A. *J. Phys. Chem. Lett.* **2010**, *1*, 1557–1562.

[49] Khara, D. C.; Samanta, A. *indian. J. Chem.* **2010**, *714*, 49A.

[50] Ito, N.; Arzhantsev, S.; Maroncelli, M. *Chem. Phys. Lett.* **2004**, *396*, 83.

[51] Maroncelli, M.; Zhang, X.-X.; Liang, M.; Roy, D.; Ernsting, N. P. *Faraday Discuss. Chem. Soc.* **2012**, *154*, 409.

[52] Roy, D.; Maroncelli, M. *J. Phys. Chem. B* **2012**, *116*, 5951–5970.

[53] Zhang, X.-X.; Liang, M.; Ernsting, N. P.; Maroncelli, M. *J. Phys. Chem. B* **2013**, *117*, 4291.

[54] Wishart, J. F.; Castner, E. W. *J. Phys. Chem. B* **2007**, *111*, 4639.

[55] Wishart, J. F.; Castner, E. W. *J. Phys. Chem. B* **2007**, *111*, 4963.

[56] Lang, B.; Angulo, G.; Vauthey, E. *J. Phys. Chem. A* **2006**, *110*, 7028.

[57] Cang, H.; Li, J.; Fayer, M. D. *J. Chem. Phys.* **2003**, *119*, 13017.

[58] Jung, Y.; Garrahan, J. P.; Chandler, D. *Phys. Rev. E* **2004**, *69*, 061205.

[59] Jung, Y.; Garrahan, J. P.; Chandler, D. *J. Chem. Phys.* **2005**, *123*, 084509.

[60] Tarjus, G.; Kivelson, D. *J. Chem. Phys.* **1995**, *103*, 3071.

[61] Mazza, M. G.; Giovambattista, N.; Stanley, H. E.; Starr, F. W. *Phys. Rev. E* **2007**, *76*, 031203.

[62] Chaudhuri, P.; Berthier, L.; Kob, W. *Phys. Rev. Lett.* **2007**, *99*, 060604.

[63] Hedges, L. O.; Maibaum, L.; Chandler, D.; Garrahan, J. P. *J. Chem. Phys.* **2007**, *127*, 211101.

[64] Léonard, S.; Berthier, L. *J. Phys.:Condens. Matter* **2005**, *17*, S3571.

[65] Garrahan, J. P.; Chandler, D. *Phys. Rev. Lett.* **2002**, *89*, 035704.

[66] Merolle, M.; Garrahan, J. P.; Chandler, D. *Proc. Natl. Acad. Sci. USA* **2005**, *102*, 10837.

[67] Widmer-Cooper, A.; Perry, H.; Harrowell, P.; Reichman, D. R. *Nature Physics* **2008**, *4*, 711.

[68] Berthier, L.; Jack, R. L. *Phys. Rev. E* **2007**, *76*, 041509–7.

[69] Rodriguez Fris, J. A.; Alarcón, L. M.; Appignanesi, G. A. *Phys. Rev. E* **2007**, *76*, 011502–6.

[70] Rodrigues Fris, J. A.; Alarcón, L. M.; Appignanesi, G. A. *J. Chem. Phys.* **2009**, *130*, 024108.

[71] Frechero, M. A.; Alarcón, L. M.; Schulz, E. P.; Appignanesi, G. A. *Phys. Rev. E* **2007**, *75*, 011502.

[72] Rodriguez Fris, J. A.; Appignanesi, G. A.; Weeks, E. R. *Phys. Rev. Lett* **2011**, *107*, 065704.

[73] Hedges, L. O.; Garrahan, J. P. *J. Phys.:Condens. Matter* **2007**, *19*, 205124.

[74] Widmer-Cooper, A.; Harrowell, P. *J. Phys.:Condens. Matter* **2005**, *17*, S4025.

[75] Plechkova, N. V.; Seddon, K. R. *Chem. Soc. Rev.* **2008**, *37*, 123–150.

[76] Weingärtner, H. *Angew. Chem. Int. Ed.* **2008**, *47*, 654–670.

[77] Kim, D.; Jeong, D.; Jung, Y. *Phys. Chem. Chem. Phys.* **2014**, *16*, 19712–19719.

[78] Park, S.-W.; Kim, S.; Jung, Y. *Phys. Chem. Chem. Phys.* **2015**, *17*, 29281–29292.

[79] Ingram, J. A.; Moog, R. S.; Ito, N.; Biswas, R.; Maroncelli, M. *J. Phys. Chem. B* **2003**, *107*, 5926–5932.

[80] Arzhantsev, S.; Jin, H.; Ito, N.; Maroncelli, M. *Chem. Phys. Lett.* **2006**, *417*, 524–529.

[81] Jin, H.; Baker, G. A.; Arzhantsev, S.; Dong, J.; Maroncelli, M. *J. Phys. Chem. B* **2007**, *111*, 7291–7302.

[82] Paul, A.; Samanta, A. *J. Phys. Chem. B* **2007**, *111*, 4724–4731.

[83] Paul, A.; Samanta, A. *Indian J. Chem., Sect. A: Inorg., Bio-Inorg., Phys., Theor. Anal. Chem.* **2010**, *49*, 649–661.

[84] Shim, Y.; Kim, H. J. *J. Phys. Chem. B* **2008**, *112*, 11028–11038.

[85] Shim, Y.; Kim, H. J. *J. Phys. Chem. B* **2013**, *117*, 11743–11752.

[86] Zhao, Y.; Hu, Z. *Chem. Commun.* **2012**, *48*, 2231–3.

[87] Terranova, Z. L.; Corcelli, S. A. *J. Phys. Chem. B* **2013**, *117*, 15659–15666.

[88] Schmollngruber, M.; Schröder, C.; Steinhauser, O. *J. Chem. Phys.* **2013**, *138*, 204504–11.

[89] Schmollngruber, M.; Schröder, C.; Steinhauser, O. *Phys. Chem. Chem. Phys.* **2014**, *16*, 10999–11.

[90] Shim, Y.; Kim, H. J. *J. Phys. Chem. B* **2007**, *111*, 4510–4519.

[91] Shim, Y.; Kim, H. J. *J. Phys. Chem. B* **2009**, *113*, 12964–12972.

[92] Lynden-Bell, R. M. *J. Phys. Chem. B* **2007**, *111*, 10800–10806.

[93] Jin, H.; Li, X.; Maroncelli, M. *J. Phys. Chem. B* **2007**, *111*, 13473–13478.

[94] Adhikari, A.; Sahu, K.; Dey, S.; Ghosh, S.; Mandal, U.; Bhattacharyya, K. *J. Phys. Chem. B* **2007**, *111*, 12809–12816.

[95] Adhikari, A.; Dey, S.; Das, D. K.; Mandal, U.; Ghosh, S.; Bhattacharyya, K. *J. Phys. Chem. B* **2008**, *112*, 6350–6357.

[96] Kimura, Y.; Suda, K.; Shibuya, M.; Yasaka, Y.; Ueno, M. *Bull. Chem. Soc. Jpn.* **2015**, *88*, 939–945.

[97] Mandal, P. K.; Sarkar, M.; Samanta, A. *J. Phys. Chem. A* **2004**, *108*, 9048–9053.

[98] Paul, A.; Mandal, P. K.; Samanta, A. *J. Phys. Chem. B* **2005**, *109*, 9148–9153.

[99] Hu, Z.; Margulis, C. J. *Acc. Chem. Res.* **2007**, *40*, 1097–1105.

[100] Nikitin, A. M.; Lyubartsev, A. P. *J. Comput. Chem.* **2007**, *28*, 2020–2026.

[101] Pronk, S.; Páll, S.; Schulz, R.; Larsson, P.; Bjelkmar, P.; Apostolov, R.; Shirts, M. R.; Smith, J. C.; Kasson, P. M.; van der Spoel, D.; Hess, B.; Lindahl, E. *Bioinformatics* **2013**, *29*, 845–854.

[102] Warshel, A. *J. Phys. Chem.* **1982**, *86*, 2218.

[103] King, G.; Warshel, A. *J. Chem. Phys.* **1990**, *93*, 8682–8692.

[104] Wu, E. C.; Kim, H. J. *J. Phys. Chem. B* **2016**, *120*, 4644–4653.

국문초록

이 논문에서는 컴퓨터 전산모사 방법을 이용해 상온 이온성 액체의 동역학에 대해 연구하였다. 먼저, 상온 이온성 액체의 굵은 입자 모형을 사용하여 동역학적 경향에 대해 알아보았다. 동역학적 경향은 각각의 이온에 대해 정해진 시간동안 동배열 앙상블에 대한 제곱 변위의 평균으로 정의된다. 온도가 낮아질 수록 동역학적 경향의 분포가 넓어지고, 특히 큰 값의 동역학적 경향을 갖는 입자들이 늘어나는데, 이는 상온 이온성 액체에서 동역학적 불균일성이 존재함을 나타내는 것이다. 이러한 현상은 음이온 보다도 특히 양이온에서 두드러지게 나타난다. 동역학적 경향이 큰 입자들은 동배열 앙상블에 대한 분산 역시 큰 값을 갖는데, 이는 동역학적 경향이 개별적인 입자들의 움직임 보다는 좀 더 긴 길이 규모에서의 이온들의 움직임과 관련이 있음을 나타낸다. 뿐만 아니라 비-가우시안 지수가 큰 입자들이 주로 동역학적 경향이 작은 입자들에서 발견되는 것으로 부터, 입자들의 움직임이 간헐적으로 일어나는 것 역시 확인할 수 있었다. 상온 이온성 액체에서 나타나는 동역학적 불균일성의 근원에 대해 알아보기 위해, 동역하적 경향과 이동도의 상관 관계에 대해서도 연구하였다. 우리는 이 연구에서 동역학적 경향과 이동도의 공간적인 분포가 상당히 일치하는 것을 관찰할 수 있었고, 이를 통해 큰 길이 규모에서 동역학적 불균일성과 계의 구조가 상관관계가 있음을 확인하였다.

이 논문의 두 번째 주제는 상온 이온성 액체의 용매화 과정에 대한 연구

로서, 들뜸 에너지가 용매화 과정의 동역학과 방출 스펙트럼에 주는 영향에 대한 연구이다. 우리는 상온 이온성 액체의 한 종류인 1-에틸-3-메틸이미다졸륨 헥사플로로포스페이트의 굵은 입자 모형을 사용하여 분자 동력학 전산모사 연구를 수행하였다. 우리는 이 연구에서 들뜸 에너지의 영향에 대해 알아보기 위해, 기존의 연구와는 달리 아주 좁은 분포를 가지는 들뜸 에너지의 분포를 사용하였다. 이를 통해 스토크스 전이 함수의 완화 과정이 들뜸 에너지를 감소시킬 수록 더 느려지는 것을 관찰하였고, 평형 상태에서 얻어진 에너지 요동의 상관 함수에 점점 더 수렴하는 것도 확인할 수 있는데,이는 들뜸 에너지가 감소할 수록 선형 응답 이론이 점점 더 잘 맞는 것을 의미한다. 다양한 경로에서 얻어지는 용매화 에너지의 분산에 대한 분석을 통해, 계의 초기 배열이 주는 영향은 1 피코초 정도의 짧은 시간동안만 존재하는 반면에, 계의 초기 속도가 주는 영향은 시간이 지날 수록 점점 증가하는 것을 확인할 수 있었다. 마지막으로 용매화 과정에서 얻어지는 방출 스펙트럼에서 적색 끝머리 효과가 나타나는 것을 관찰하였는데, 기존의 다른 방법을 이용한 연구 결과와 일치하는 것도 확인할 수 있었다.

주요어: 상온 이온성 액체, 동역학적 불균일성, 동배열 앙상블, 굵은 입자 모형, 동역학적 경향, 용매화 동역학, 스토크스 전이 함수, 적색 끝머리 효과, 분자 동역학 전산모사

학번: 2007-20295